Kalliopi Kanaki

Electric Field and Drift Characteristics Studies for the Multiwire Chambers of the Third Plane of HADES

Kalliopi Kanaki

Electric Field and Drift Characteristics Studies for the Multiwire Chambers of the Third Plane of HADES

Contents

List of Figures

1 Introduction

The investigation of the properties of nuclear matter over a wide range of temperature and density is one of the major topics of contemporary nuclear physics. The main motivation for this is the unique opportunity to investigate the equation of state (EOS) of nuclear matter and to test the predictions of the fundamental theory of strong interactions, quantum chromodynamics (QCD): deconfinement and the *quark-gluon plasma*, as well as the intimately related restoration of *chiral symmetry*. The EOS of strongly interacting matter is of importance for astrophysical problems like neutron stars and supernovae, as well as Big Bang nucleosynthesis and related topics [1].

QCD attempts to describe nuclear matter as the interaction of quarks through the exchange of colour force carriers called gluons. It leads to the conclusion that isolated single free quarks or gluons cannot be observed. Quarks and gluons appear only in colourless hadronic bound states, such as baryons and mesons (confinement), which are the effective degrees of freedom in slightly compressed and heated nuclear matter in a confinement state. The situation changes at very high densities and temperatures ($\rho \geq 5\rho_0$[1] or T $\geq$ 170 MeV), where one expects the transition of nuclear matter to the quark-gluon plasma, where quarks and gluons become deconfined. This is schematically displayed in Fig. 1, where the cross-hatched region indicates the transition from confined to deconfined strongly interacting matter. The dashed curve depicts a possible phase border line. Fig. 1 also shows the results of experiments performed at different beam energies.[2] As we see in the phase diagram, the chemical and thermal freeze-out curves merge at SIS energies. The corresponding matter state is clearly within the confinement region. In this energy regime, the achieved states of strongly interacting matter consist of nucleons which are excited into baryonic resonance states to a substantial fraction (such as Δ and N^*), along with accompanying meson production, mainly pions. The corresponding region in the phase diagram is therefore often referred to as region of hadronic resonance matter. The importance of studying hadronic matter is evident, as it is the final state

---

[1]$\rho_0 = 0.17$ fm^{-3} is the saturation density of symmetric nuclear matter.

[2]The accelerators SIS (S̲chwerI̲onen S̲ynchrotron at GSI, Darmstadt), AGS (A̲lternating G̲radient S̲ynchrotron at Brookhaven National Laboratory, Long Island), SPS (S̲uper P̲roton Synchrotron at the European Research Laboratory CERN in Geneva), and RHIC (R̲elativistic H̲eavy-I̲on C̲ollider at Brookhaven National Laboratory, Long Island) deliver heavy-ion beams with energies up to 4(Z/A)GeV, 29(Z/A)GeV, 400(Z/A)GeV and $\sqrt{s} = 200$ AGeV respectively. Z(A) denotes the charge (mass number) of the projectile nuclei.

before freeze-out of resonance matter and any possibly produced quark-gluon plasma state. Only with higher beam energies, say such ones which at least are available at AGS, the deconfinement region can be reached.

The other forementioned important consequence of QCD is the spontaneous breaking of chiral symmetry in the ground state resulting in a non vanishing scalar quark condensate, $\langle \bar{q}q \rangle \neq 0$. Lattice QCD calculations predict a partial restoration of chiral symmetry with increasing density ρ and temperature T. As a result one should expect that some properties of light hadrons, such as masses, spectral functions and couplings, change considerably in the nuclear environment, where the chiral condensate is expected to be reduced.

Various experiments have been performed to confirm or reject theoretical predictions, among them the one suggested by Brown and Rho [2], according to which masses of non-strange hadrons such as nucleons, ρ and ω mesons are reduced in the nuclear medium close to a proportionality to the in-medium quark condensate $\langle \bar{q}q \rangle$. Unfortunately, the conjectured direct relation of the quark condensate to physical observables has not been rigorously established. For instance, QCD sum rules relate the vector meson masses, in zero-width approximation, not only with the chiral condensate but also with other condensates, momenta of parton distributions and forward scattering amplitudes. However, such and other models, based on the principles of chiral symmetry in strongly interacting systems, predict substantial changes of hadron properties in dense matter. One and obviously the most direct way to probe the predicted in-medium modifications is by studying the dilepton decays of vector mesons in the hot and dense nuclear matter (this will be described in more detail in section 3).

A series of pioneering dilepton experiments has already been performed at SIS energies. These, and complementary experiments at larger energies, will be described in section 2. The unresolved problems of the first generation experiments will be further studied by HADES (High Acceptance Di-Electron Spectrometer) which is installed at GSI in Darmstadt. HADES will use the pion, proton and heavy-ion beams delivered by the SIS to produce baryon-dense and not too hot matter. According to present models (see Appendix), the chiral condensate is most sensitive to changes of the density, therefore one expects valuable insights at these energies. (On the contrary, at relativistic beam energies hot and baryon-poor matter is produced and deconfinement effects are envisaged to be probed.)

The aim of this report is a brief presentation of the physics motivation that lies behind the HADES project, and in more detail, the description of the main features of the spectrometer. More explicitly, it will deal with the operational features of the drift chambers which are incorporated in the
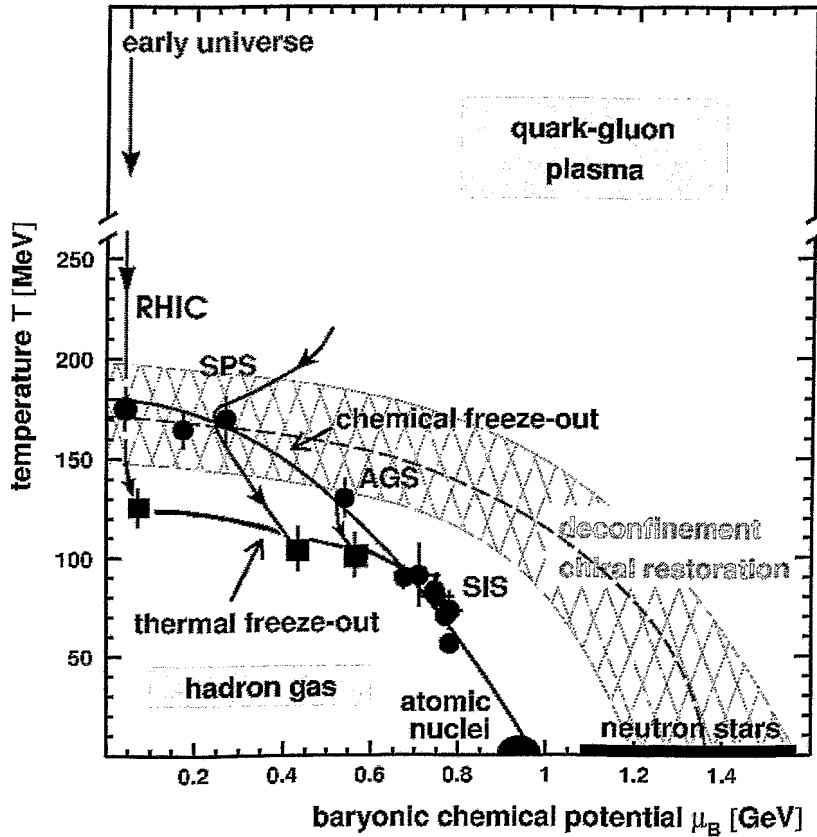
Figure 1: Schematic phase-diagram of strongly interacting matter. Depicted are lines of chemical and thermal (kinetic) freeze-out and corresponding results from various accelerators. The chemical freeze-out parameters are deduced from hadron yields, while the thermal freeze-out parameters result from analyses of transverse momentum spectra. The cross-hatched area indicates the region of the outset of deconfinement and chiral symmetry restoration.

experimental setup. The studies of the working characteristics and the simulations aimed to optimize the performance of the drift chambers are also described. Finally mentioned are the conclusions of these simulations and the proposals that will indeed lead to the optimization of the operation of the drift chambers.

2 First generation experiments with dileptons

Many hadronic observables have been measured in heavy-ion collisions up to now: hadron multiplicities, rapidity distributions, transverse momentum spectra, flow observables like side flow, squeeze and elliptic flow and two-(three-) body correlations as well. These observables are sensitive to certain stages of the collision. Rapidity distributions, transverse momentum spectra and correlations are thought to reflect the kinetic freeze-out, where the hadronic strong interactions cease. Multiplicities and their ratios reflect the chemical equilibration and might be sensitive to certain early stages. Flow effects, mainly the elliptic flow, are caused by the pressure of early times; but also geometrical shadowing effects affect these observables. For a recent survey we refer the interested reader to [3].

Among the probes of heavy-ion collisions are real and virtual photons. Virtual photons decay into a lepton pair. As leptons do not undergo strong interactions but interact only weakly and electromagnetically, they are considered unique observables for studying the evolution and dynamics of ultra-relativistic heavy-ion collisions from the hottest and densest early stages till freeze-out. Thus, the region above the freeze-out curves in Fig. 1 becomes directly accesible. Furthermore, dileptons offer the opportunity to have a particularly interesting access to the vector mesons through their leptonic decays. This, in turn, is of particular importance with regard to the ρ meson. Due to its very short lifetime (see Tab. 1) compared to the typical fireball lifetime (10 - 15 fm/c), most of the ρ mesons produced in the collision will decay inside the interaction region. If the temperature and/or the baryon density are high enough for partial chiral symmetry restoration to take place, the ρ mesons will decay with a changed spectral function leading to a detectable signal in the low-mass dilepton spectrum.

meson	mass (MeV/c^2)	width (MeV/c^2)	lifetime τ (fm/c)	e^+e^- branching ratios
ρ	768	152	1.3	4.4×10^{-5}
ω	782	8.43	23.4	7.2×10^{-5}
ϕ	1019	4.43	44.4	3.1×10^{-4}

Table 1: Characteristic quantities of light vector mesons.

In such a way in the early nineties, the hope was born to verify explicitly the mass change of the ρ meson in strongly interacting matter. It was

supposed that the ρ meson mass is directly related to the chiral condensate. Therefore, by quantifying a change of the ρ meson via the dielectron decay channel, one is able to measure directly the change of the chiral condensate.

It turned out, however, in more recent studies that the mass-chiral condensate relation might not be so direct, and other effects influence the effective in-medium mass. Since the ρ meson has a large width, which is expected to be further enlarged by conventional interactions, it might be difficult to identify the in-medium ρ signal [4]. Properly speaking, instead of characterizing the ρ meson as a quasi-particle with a mass and width, it turned out that it is more appropriate to deal with a spectral function which encodes the excitations with quantum numbers of the ρ. Basically, similar ideas apply to ω and ϕ mesons which however can still survive as narrow quasi-particle excitations.

In practice there are a few things making electromagnetic probes rather difficult:

1. There are several competing background processes generating dielectrons: bremsstrahlung and Dalitz decays of Δ, ω, ρ, ϕ, η, π. These decays produce e^+e^- pairs mainly in the low-mass region. Dalitz decays of higher baryon resonances can become sizeable.

2. Although with dielectrons one is monitoring the full time evolution of strongly interacting matter, the finally observed spectra consist of a convolution of all stages with the local emission strength. This makes the deconvolution difficult.

3. Experimentally, electromagnetic signals are rare probes due to their small branching ratios (see Tab. 1).

It is, therefore, natural that the first heavy-ion collision experiments with dileptons had several problems which must be overcome by improved experimental devices. Let us briefly mention the first generation experiments.

2.1   CERES experiments at CERN-SPS

A direct evidence for a dropping ρ meson mass seems to be provided by the enhanced production of dileptons with invariant masses around 400 - 500 MeV/c^2 above known sources of dileptons in the CERES/NA45 experiments of heavy-ion collisions at CERN-SPS. The experiments cover beam energies of 40, 80, 158 and 200 AGeV with sulphur and lead projectiles on gold targets.
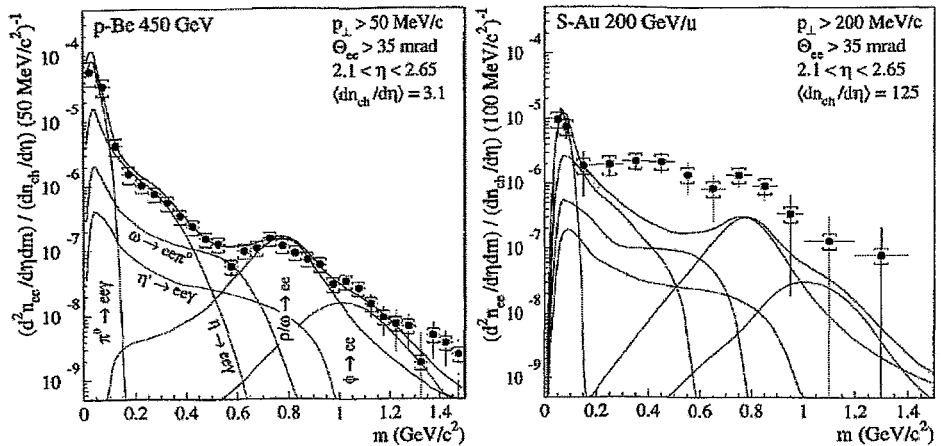
Figure 2: Invariant mass spectra of inclusive e^+e^- pairs in p(450 GeV) + Be (left) and S(200 AGeV) + Au (right) collisions showing the data (full circles) and the various contributions from hadron decays. Systematic (brackets) and statistical errors (bars) are plotted independently of each other [5].

The investigation primarily concerned the production of electron-positron pairs and searched for direct photons in proton-nucleus and nucleus-nucleus collisions. The experiment studied the continuum in the mass region up to 1.2 GeV/c^2 and the vector mesons ρ, ω and ϕ. The produced matter was meson rich ($N_\pi : N_B \sim 6 : 1$). In the first phase (NA45/1) it was concluded that there is a significant excess, by a factor of about 5, of dielectron pairs in the mass range between 0.2 and 1 GeV/c^2 in S + Au collisions at 200 AGeV at central rapidities, as compared to the hadronic background extracted from p + Be and p + Au collisions (see Fig. 2). For the proton induced interactions the low-mass spectra are satisfactorily explained by electron pairs from hadron decays [5]. The pion annihilation channel has been included in most of the calculations, on top of the hadronic sources. The collision dynamics has been treated in a variety of approaches, assuming the formation of a hadronic system in thermal equilibrium [7] or without equilibrium [8], including transport models which explicitly propagate baryons and mesons, models based on a thermalized hadronic gas [9], and models concerning the inclusion of semi-leptonic decays of open charm mesons to the hadron decay contributions and using the "quark-hadron duality" [10].

For the lead beam program the experiment was upgraded in steps. The latest results showed that in Pb + Au collisions at 158 AGeV there is also

6

an enhancement of the number of dielectrons in the mass region below the vacuum ρ peak by a factor of 2.6 ± 0.5 (stat.) ± 0.5 (syst.) (see Fig. 3); this enhancement grows steeper than linearly with the charged particle multiplicity in the event.

Other dilepton experiments of CERN-SPS (HELIOS, NA38/50/60) addressed the intermediate and large-mass region. Since we are here interested in the low-mass region up to invariant masses of the ϕ meson, we do not describe them.
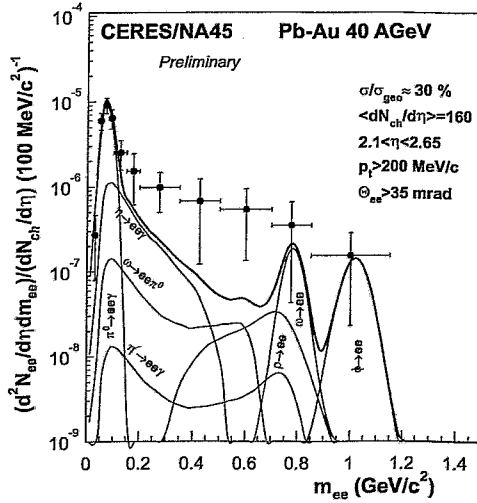
Figure 3: Inclusive invariant e^+e^- mass spectrum in 158 AGeV Pb + Au collisions normalized to the observed charged-particle density. The full line represents the e^+e^- yield from hadron decays scaled from p-induced collisions. The contributions of individual decay channels are also shown [6].

2.2   Dilepton experiments at the Bevalac

Dileptons have also been measured in heavy-ion collisions with the accelerator Bevalac at Berkeley (CA, USA) by the DLS[3] collaboration at incident energies that were two orders of magnitude lower than those at SPS, i.e. in the energy regime of SIS. The measurements concerned dielectron production in p + p and p + d collisions with beam kinetic energies from 1.04 to 4.88 GeV, Ca + Ca at 1 and 2 AGeV and also systems such as C + C,

---

[3]DiLepton Spectrometer

7

d + Ca and He + Ca. In contrast to the CERES experiment, the produced matter was baryon rich ($N_\pi : N_B \sim 1 : 6$). For the Ca + Ca system the data lead to a dilepton production cross section which is up to 7 times larger than predicted by conventional models (see Fig. 4). This discrepancy between experiment and theory based on a cocktail of free hadronic sources of e^+e^- pairs is particularly visible in the intermediate invariant mass range $200~\mathrm{MeV/c^2} < \mathrm{M} < 600~\mathrm{MeV/c^2}$, which is just below the ρ/ω meson pole mass. It could be significantly reduced by more refined transport calculations [11] in which the in-medium spectral function of the ρ meson is included. Nevertheless, an enhancement of about a factor 3 remains in this mass range [12].
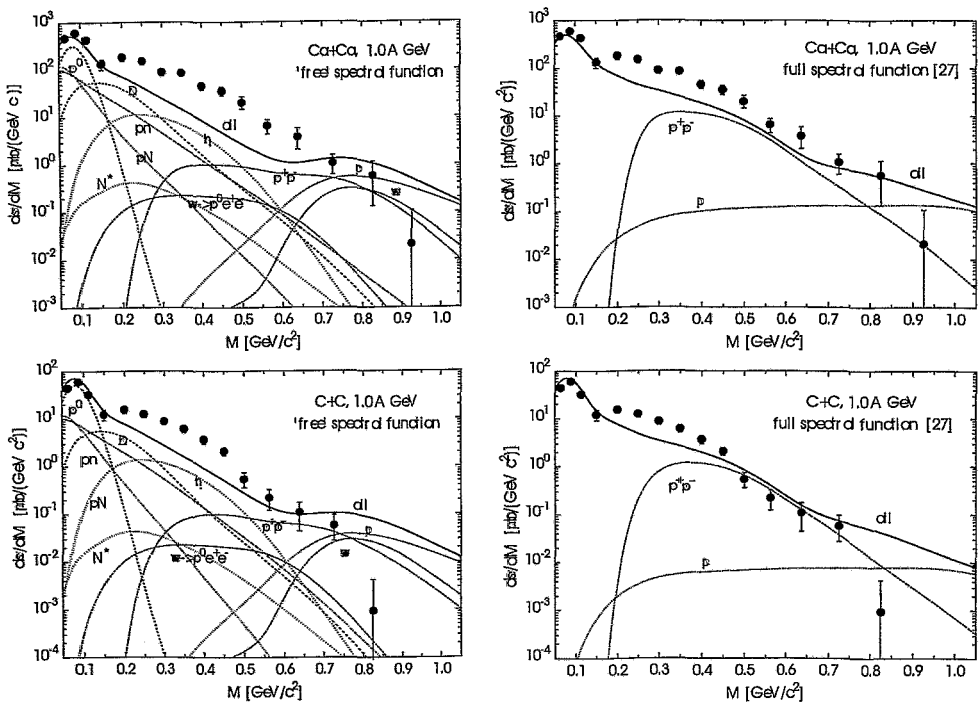
Figure 4: Differential cross sections (full circles) for dielectron production measured by the DLS [12] collaboration in comparison to BUU transport calculations (full line) [11]. The spectra on the left depict the yields from individual contributing sources which have been calculated using "free" spectral functions for decays in vacuum. On the right shown are the yields from ρ decay and $\pi^+\pi^-$ annihilation which have been calculated using in-medium spectral functions; the other sources are not shown.

Up to now the discrepancy between data and transport calculations with many different assumptions could not be resolved. Any interpretation has to take into account two other experimentally verified facts. First, the large e^+e^- yield below M < 550 MeV/c^2 cannot be attributed to an enhanced η Dalitz decay contribution, since such an assumption would contradict the measured η meson production cross sections for C + C and Ca + Ca collisions. Second, the measured dilepton spectra from elementary p + p collisions are reasonably well reproduced by the transport model approaches. Therefore, the dilepton enhancement observed already in the light ion collisions investigated at the Bevalac might be a first hint for in-medium modifications.

3 HADES: A High-Acceptance Di-Electron Spectrometer

3.1 Physics motivation

The High Acceptance Di-Electron Spectrometer (HADES) at GSI, Darmstadt, provides the possibility for electron-positron pair spectroscopy at incident energies up to 2 AGeV. These energies together with a proper choice of the collision system allow access to a wide region in the nuclear matter phase diagram ranging from ground state matter density ρ_0 up to $3\rho_0$ and temperatures up to 100 MeV. The long range physics program of HADES includes the systematic studies of e^+e^- pair production in hadron and heavy-ion induced collision systems and to look for precursor effects of chiral symmetry restoration. The SIS delivers as projectiles pions with a momentum range from 0.6 to 2.8 GeV/c, protons and heavy ions at beam energies up to 4.7 GeV and 2 AGeV respectively. In the first time of operation, HADES will identify ρ, ω and ϕ decays and search for shifts of the corresponding "spectral lines". In parallel the continuum below the ρ/ω peak will be addressed to resolve the DLS puzzle. Besides the heavy-ion collisions, a focus will be on elementary hadronic reactions, such as $\pi + N$, to study more recent problems like $\rho - \omega$ interferences, which require quite subtle experiments.

Another important motivation concerns the measurement of electromagnetic form factors of mesons and baryons, such as the ω transition form factor, using the secondary pion beam facility of SIS. Knowledge of such properties is very significant for the theoretical models of hadrons, since the form factors carry complete information on the electromagnetic structure of the particles [13].

A schematic view of the spectrometer is depicted in Figs. 5 and 6. Starting from the side of the beam, visible are the Ring Imaging Cherenkov counter (RICH), the inner two planes of multiwire drift chambers (MDC), the magnet coils, the outer two planes of MDC, the Time of Flight wall (TOF) and finally the Pre-Shower detectors.

3.2 Invariant mass spectra

The electron-positron pairs produced by the decay of vector mesons and other processes will be used for the reconstruction of the *invariant mass spectra*. Fig. 7 depicts some processes that lead to dilepton production. All four processes include the production of a virtual photon, which decays into the dileptons we measure. Later on, what we refer to as mass, momentum and
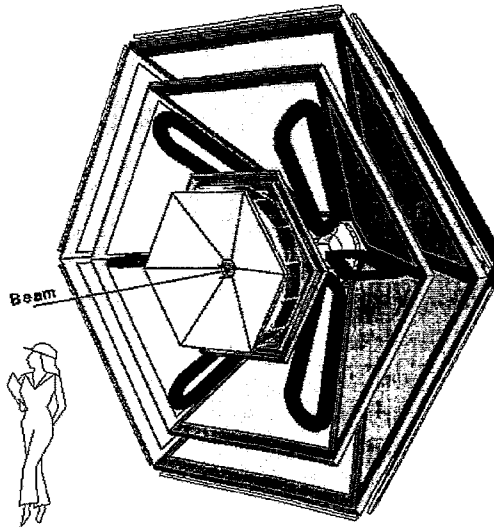
Figure 5: Front view of the HADES spectrometer.
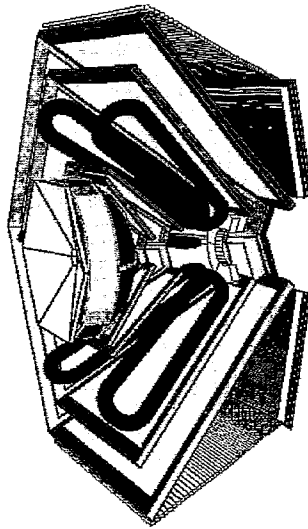
Figure 6: Side view of the HADES spectrometer.

all the kinematic variables of the dilepton are in respect to this virtual pho-

ton. According to the Vector Dominance Model, the virtual photon couples directly to the vector mesons. This is particularly important for the pion annihilation process $\pi^+\pi^- \to \rho \to \gamma^* \to e^+e^-$. A change of the properties of the ρ meson, therefore, becomes directly accessible through the e^+e^- pair. Similar considerations hold for the ω and ϕ mesons which are, however, produced in other processes. While such pure s channel processes refer directly to the strength ("mass") distribution of the original ρ, ω and ϕ mesons, the other processes depicted in Fig. 7 cause wider continuum distributions of the resulting e^+e^- pairs.
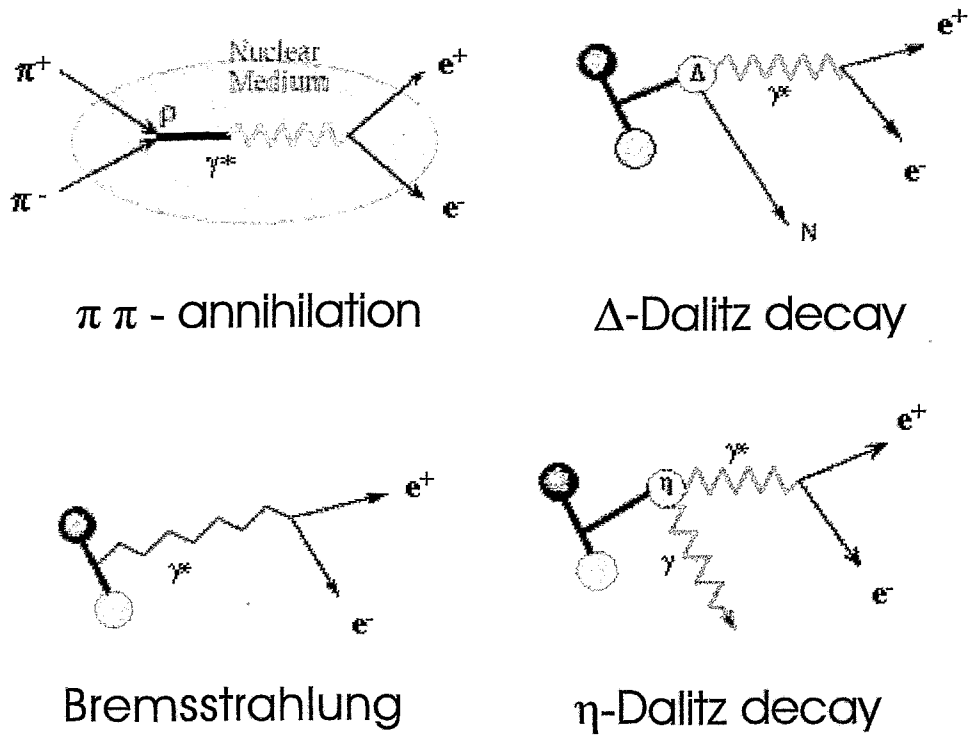
Figure 7: Schematic illustration of processes of dilepton production.

In the case of the $\pi^+\pi^-$ annihilation, the knowledge of four-momenta of both particles provides us the possibility to calculate the original ρ mass. The invariant mass of a e^+e^- pair is defined as:

$$M = \sqrt{P_\mu(e^+ + e^-)P^\mu(e^+ + e^-)}, \tag{1}$$

where $P^\mu = p^\mu(e^+) + p^\mu(e^-)$ is the four-vector for the e^+e^- pair. Einstein's sum convention is employed for Lorentz indices. Spelling out the above term

by using the components of the four-vector $P^{\mu}(e^+e^-) = (E_{e^+} + E_{e^-}, \vec{p}_{e^+} + \vec{p}_{e^-})$, we get

$$M = \sqrt{E_{e^+}^2 + E_{e^-}^2 + 2E_{e^+}E_{e^-} - |\vec{p}_{e^+}|^2 - |\vec{p}_{e^-}|^2 - 2\vec{p}_{e^+} \cdot \vec{p}_{e^-}}. \qquad (2)$$

For electron and positron energies above some hundred MeV, as in our case, the masses can be neglected: $\sqrt{|\vec{p}_{e^\pm}|^2 + m_0^2} \approx \sqrt{|\vec{p}_{e^\pm}|^2} = p_{e^\pm}$. Eq. 2 is thus simplified to

$$M = \sqrt{2p_{e^+}p_{e^-} - 2\vec{p}_{e^+} \cdot \vec{p}_{e^-}}. \qquad (3)$$

Replacing the scalar product with the use of the angle α between the two three-momentum vectors, we can write

$$
\begin{aligned}
M &= \sqrt{(E_{e^+} + E_{e^-})^2 - (\vec{p}_{e^+} + \vec{p}_{e^-})^2} \\[2mm]
&= \sqrt{2p_{e^+}p_{e^-} - 2p_{e^+}p_{e^-}\cos\alpha} \\[2mm]
&= \sqrt{2p_{e^+}p_{e^-}(1 - \cos^2(\alpha/2) + \sin^2(\alpha/2))} \\[2mm]
&= \sqrt{2p_{e^+}p_{e^-}\, 2\sin^2(\alpha/2))} \Rightarrow \\[2mm]
M &= 2\sqrt{p_{e^+}p_{e^-}}\,\sin(\alpha/2). \qquad (4)
\end{aligned}
$$

So, in order to determine the invariant masses of the dileptons, the momenta $p_{e^\pm}$ of the pair, as well as its opening angle α are required. Note that by definition the invariant mass is Lorentz invariant. The momenta $p_{e^\pm}$ and the angle α are measured in a common reference frame.

Generally, a dilepton invariant mass spectrum will consist of a smooth background, with several peaks sitting on it. As an illustrative example, we depict model calculations in Fig. 8 from the HADES proposal [14].

The spectrum is expected to be quite steep. The first steps of HADES operation will be devoted to identify the contributions from ρ, ω and ϕ decays, which are seen as the pronounced peaks.

For the identification of the different mesons in the mass spectra the e^+e^- resolution should be optimised. Especially in the mass region of ρ and ω, $\Delta M/M$ must be appropriate to resolve the resonance width of ω, i.e. it should be approximately 1 % (see Tab. 1).
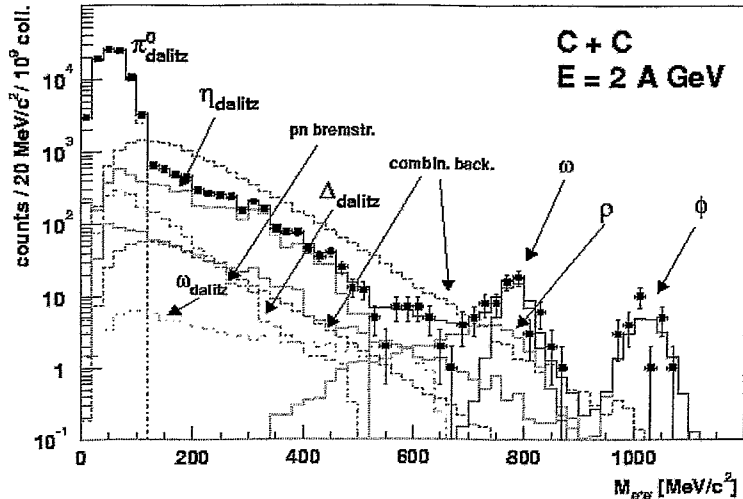
Figure 8: Simulated invariant mass spectrum of e^+e^- pairs for C + C at $E_{kin} = 2$ AGeV. Various individual contributions are separately depicted. A total yield (squares and solid histogram) of approximately 180.000 pairs is expected for $2 \cdot 10^9$ semicentral collisions ($\approx 40\%$ of the total cross section) and for full azimuthal coverage setup with 3 MDC planes. In the ρ/ω mass region about 180 counts are expected. The combinatorial background is calculated for two scenarios of close pair rejection. The upper curve corresponds to double ring recognition in the RICH only (worst case), the lower curve to ideal double track resolution (best case). Due to the high position resolution of the MDC planes the expected yield will come close to the lower curve. The total dielectron yield is obtained with the lower curve [14].

3.3   Requirements to the detector system

In order to solve the puzzling results of the first generation experiments, mainly from DLS as mentioned above, the resolution and count rates must be substantially improved. The resulting requirements of the HADES spectrometer are:

- *Count rate stability*

  The vector mesons ρ, ω and ϕ which we are interested in, decay into dileptons with branching ratios of order of magnitude 10^{-4} (see Tab. 1). In order to be able to detect such pairs with good statistics, a high

14

reaction rate is required. As a consequence the detectors should be able to handle so high rates.

- *Mass resolution*

  As mentioned above, the mass resolution should be $\Delta M/M \simeq 1\%$.

- *Track resolution*

  Electron-positron pairs are not only created by the decay of vector mesons but also by many other processes. Pairs could be even stem from an electron and a positron from different conversion processes, say a positron from an external conversion and an electron from a π^0 Dalitz decay, or a positron from a π^0 Dalitz decay and an electron from Compton scattering of a γ quantum. In order to suppress this combinatorial leptonic background, it is necessary to reconstruct all the trajectories of dileptons. This requires a high track resolution and geometric acceptance of the detector system, in combination with the use of low material quantity to diminish the scattering and the secondary reactions of the e^+e^- pairs.

- *Solid angle acceptance*

  For the maximization of the number of dileptons to be detected the spectrometer acceptance should cover a big solid angle. This is achieved by the concept of rotational symmetry. The covered solid angle amounts roughly to 2π.

4   Description of the spectrometer

Fig. 9 depicts a schematic view of the HADES detector system. The system is divided into 6 identical sectors surrounding the beam axis; the picture shows a two-dimensional slice to demonstrate the large angular acceptance of HADES, which stretches between 16° and 88°. HADES is comprised of the components which are described in detail below.
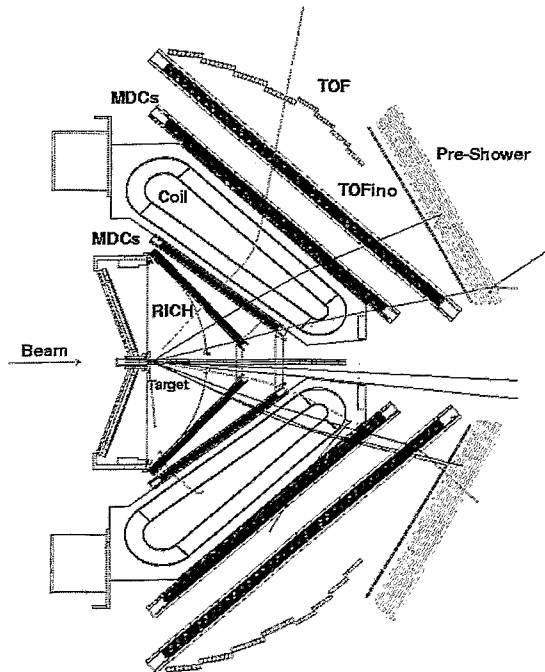
Figure 9: Schematic cross section along the y-axis of the HADES spectrometer. The magnet coils are projected onto the *(y, z)* plane.

4.1   Start Detectors

Two identical 8-strip diamond detectors of octagonal shape are placed 75 cm downstream and 75 cm upstream of the HADES target. The downstream detector will veto all particles with no reaction with target nuclei to provide a start signal with a rate of more than 10^7 particles/s. The widths of the strips are optimized such that a coincidence of one start strip with 3 veto strips is sufficient for a veto efficiency of 96.5%.

4.2 Ring Imaging Cherenkov Counter

The Ring Imaging Cherenkov (RICH) detector is a device for electron and positron identification. In the SIS energy regime, electrons and positrons emitted in nuclear collisions have velocities $\beta = v/c \rightarrow 1$, while all hadrons have $\beta < 0.95$. The Cherenkov effect can be used to distinguish electrons from hadrons and to obtain a trigger signal for events containing e^+e^- pairs. For a radiator gas with proper refraction index the detector is hadron blind and the Cherenkov opening angle is constant for leptons with $\beta > 0.95$.

4.3 Superconducting Toroidal Magnet

The superconducting toroidal magnet consists of 6 coils in separate vacuum chambers. The coil cases are aligned with the frames of the MDCs and all other segmented detectors to reduce dead space in the spectrometer. The magnet provides the momentum kick which is necessary for a resolution of about 1 % of charged particle momenta.

4.4 Multiwire Drift Chambers

The HADES tracking system consists of four drift chamber planes (I-IV), two before and two behind the field area of the superconducting toroid. Each chamber plane is composed of six trapezoidal modules and has the shape of a frustrum. A module covers 60° of azimuthal angle and four modules of the detectors I to IV each form a sector. Module sizes range from 88 cm × 80 cm to 280 cm × 230 cm (height times larger baseline). A chamber module is composed out of six drift cell layers. The cell sizes vary from 5 × 5 mm^2 to 14 × 10 mm^2 from detector I to IV to achieve a constant granularity. The cells are formed by interspersed sense and field wires and cathode wire planes. The total number of drift cells is approximately 27,000.

4.5 Time-of-Flight Wall

The Time-of-Flight (TOF) wall is made of six sectors in hexagonal geometry, each one constituted by thirteen cases containing eight scintillating bars. Each bar will be read out at the two ends by fast photomultipliers, in order to reconstruct with a good accuracy the time of flight from the target ($\sigma_t = 100$ - 150 ps) and the hit position along the bar itself ($\sigma_x = 1.5$ - 2.3 cm). For acceptance at forward angles another set of six TOF sectors is installed before the Pre-Shower detectors. The TOF main tasks are to measure the hadron

multiplicity, so as to trigger on the centrality of heavy-ion collision and to perform the electron/hadron discrimination.

4.6   Pre-Shower Detectors

The basic idea of electron identification is to measure electromagnetic showers produced in lead material. The HADES pre-shower detectors consist of two lead converters inserted between three wire chambers with pad read-out. Shower recognition is performed by comparing the number of particles measured before and after the lead converters. In the case of hadrons this ratio is close to 1. Particle hits are identified via charge produced in ionization processes in the wire chambers working in the self-quenching streamer (SQS) mode. The main advantage of the SQS mode is that the induced charge is nearly independent of the particle's specific energy loss and, therefore, low energy protons do not produce large signals in the post converter chambers because of their significant energy loss in the lead material and finally are not misidentified with electromagnetic showers. The shower detectors together with the TOF form the Multiplicity Electron Trigger Array (META).

5 The HADES trigger concept

The reason for the existence of the HADES trigger system is the identification of dielectron events. Its main task is the on-line selection of such events that contain a dilepton. There are three trigger levels which contribute to the above discrimination.

5.1 First level trigger

At this stage a fast hardware selection of central collisions takes place employing the multiplicity information from the TOF. When the multiplicity exceeds a defined threshold, the event is considered to be central. Via this discrimination the primary event rate is reduced by a factor of 10. Involved in this level are also the Start and Veto detector, in combination with the META components.

5.2 Second level trigger

The pair of rings in the RICH that correspond to the production of a dilepton event is combined with the corresponding signals detected by the META system by using the time of flight information. This is the principle of the second level trigger. The angle region where the dilepton identification takes place is above 45°. Below this angle the discrimination becomes less effective due to the existence of fast pions. For this reason the information about characteristic electromagnetic showers caused by dileptons is used. At this stage, both software and hardware methodes are employed. Thus, a further reduction of the event rate takes place by a factor of 100.

5.3 Third level trigger

The dedicated software of the last level will correlate events from the drift chambers with events from the shower detectors and rings from the RICH. Thus, a further suppression of the false coincidences over the true ones will be achieved. The reduction of the event rate is by a factor of 10.

6   Multiwire Drift Chambers

The main part of this report is dedicated to the description of the construction, operation and studies of characteristics of drift chambers. More specifically, in the next chapters described are the procedure of manufacture of the detectors, their main operational characteristics, the tests that were performed to study these characteristics and finally, some simulations concerning the behaviour of the electric field in the interior of the chambers.

6.1   Principle of operation

A drift chamber is a gaseous detector that allows the determination of spatial coordinates of trajectories created by charged particles which traverse its active volume, resulting in excitation and ionization of the atoms of the medium. Of all possible interactions only the electromagnetic one is generally used as a basis for detection, being many orders of magnitude more probable than strong or weak interactions [15].

On the passage of the particle, a discrete number of primary ionizing collisions takes place which liberate electron-ion pairs in the medium. The electrons ejected are accelerated by the field towards the anodes and can have enough energy (larger than the ionization potential of the medium) to further ionize, producing secondary electron-ion pairs; the sum of the two contributions is called total ionization. The total number of electron-ion pairs can be expressed by $n_T = \Delta E / W_i$, where ΔE is the total energy loss in the gas volume considered and W_i is the effective average energy to produce one pair.

An expression for the average energy loss per unit length due to Coulomb interactions has been obtained by Bethe and Bloch in the framework of relativistic quantum mechanics

$$\frac{dE}{dX} = -K\frac{Z}{A}\frac{\rho}{\beta^2}\Big[\ln\frac{2mc^2\beta^2 E_M}{I^2(1-\beta^2)} - 2\beta^2\Big], \quad K = \frac{2\pi N z^2 e^4}{mc^2}, \tag{5}$$

where N is the Avogadro number; m and e denote the electron mass and charge; Z, A, and ρ stand for the atomic number and mass, and the density of the medium respectively; I is its effective ionizing potential; z is the charge and β the velocity of the projectile. The quantity E_M represents the maximum energy transfer allowed in each interaction. Inspection of the above formula shows that the differential energy loss depends only on the projectile velocity β and not on its mass. After a fast decrease dominated by the β^{-2} term, the energy loss reaches a constant value around $\beta \approx 0.97$ and eventually slowly increases for $\beta \to 1$ (relativistic rise).

As described above, along the particle trajectory the formation of localised groups of electrons, called *clusters*, takes place. In typical drift chamber gases they consist of one to three electrons. The primary ionization encounters, being a small number of independent events, follow Poisson-like statistics. In a classical formulation due to Landau, the energy loss distribution can be written as

$$f(\lambda) = \frac{1}{\sqrt{2\pi}} e^{-\frac{1}{2}(\lambda + e^{-\lambda})},$$ (6)

where the reduced energy variable λ represents the normalized deviation from the most probable energy loss $(\Delta E)_{mp}$,

$$\lambda = \frac{\Delta E - (\Delta E)_{mp}}{\xi}, \quad \xi = K \frac{Z}{A} \frac{\rho}{\beta^2} X,$$ (7)

with ΔE being the actual loss and ξ the average energy loss given by the first term of the Bethe-Bloch formula Eq. 5.

In the HADES drift chambers the gas mixture used consists of 60 % He and 40 % isobutane. In pure helium the number of electron-ion pairs created per unit length is $n_T(He) = 7.8$, while for isobutane it is $n_T(iC_4H_{10}) = 195$. That gives a total number of electron-ion pairs per unit length for the gas mixture equal to $n_T(He - iC_4H_{10}) = \frac{1}{6} n_T(He) + \frac{1}{4} n_T(iC_4H_{10}) = 83$. The majority of the pairs are produced by isobutane and not by the main gas of the mixture.

6.2 Interactions of photons in gas media

As for charged particles, an electromagnetic interaction allows the detection of photons; in this case, however, the interaction is a single localized event. The probability of absorption can be written in terms of cross section σ. The attenuation of a beam of photons traversing a thickness X of a medium having N molecules per unit volume is given by

$$I = I_0 e^{-\sigma N X} = I_0 e^{-\mu x}.$$ (8)

The mass attenuation coefficient is usually denoted by $\frac{\mu}{\rho}$, where ρ is the material density and μ is the linear attenuation coefficient giving $I = I_0 e^{-\mu X}$.

21

There are three different ways for a photon to interact with matter:

- Photoelectric effect

  Photoelectric absorption is a quantum process involving one or more transitions in the electron shells of a molecule. Denoting by E_j the energy of a shell j, photoelectric absorption can take place only for photon energies $E_\gamma \geq E_j$ and at a given energy the contributions of all levels having $E_j < E_\gamma$ add up. The absorption is maximum at the edge and then very rapidly decreases with energy. The photoelectric effect results in the emission of a photoelectron of energy $E_e = E_\gamma - E_j$; the excited molecule can then return to its ground state mainly through two competing mechanisms:

  fluoresence, i. e. the transition of an electron from an energy shell $E_i < E_j$ into the j-shell, with the emission of a photon of energy $E_j - E_i$;

  radiationless transition, or Auger effect, which is an internal rearrangement involving several electrons from the lower energy shells with the emission of an electron of energy very close to E_j.

  The non-relativistic Born approximation gives a cross section of $\sigma_{\rm ph} = \sqrt{\left(\frac{32}{\epsilon^7}\right)}\alpha^4 Z^5 \sigma_{\rm Th}^{\rm e}$, where $\epsilon = E_\gamma/m_e c^2$ is the reduced photon energy and $\sigma_{\rm Th}^{\rm e} = 6.65 \times 10^{-25}$ cm^2 is the Thomson cross section for elastic scattering of photons on electrons.

- Compton effect

  When the photon energy rises well above the highest atomic energy level, Compton scattering begins to be the dominant process. The incident photon with energy $h\nu_0$ is scattered by a quasi-free electron by an angle θ and gets a new energy $h\nu'$ such that

  $$\frac{1}{h\nu'} - \frac{1}{h\nu_0} = \frac{1}{mc^2}(1 - \cos\theta). \tag{9}$$

- Pair production

  At the presence of a Coulomb field it is possible for photons to produce an electron-positron pair. This process is kinematically allowed for photon energies $E_\gamma \geq 2m_e c^2 + 2\frac{m_e^2}{m_{nuc}}c^2$. The cross section of this process is proportional to Z^2, so it is more probable to happen in the Coulomb field of a nucleus than in the field region of an electron.

6.3 Ion and electron diffusion

The read-out of the drift chambers results in time information which corresponds to the drift time of the primary electrons from the location of their creation to the closest sense wire. The arrival of these electrons determines the beginning of the signal. But since we are interested in spatial information, the knowlegde of the drift velocity behaviour inside the drift cells is of great importance. This behaviour depends on the drift properties of ions and electrons in the gas medium of the chamber.

6.3.1 Ion and electron diffusion without electric field

Charges produced by an ionizing event quickly lose their energy in multiple collisions with the gas molecules and assume the average thermal energy distribution of the gas. Simple kinetic theory provides the average value of the thermal energy, $\epsilon_T = (3/2)kT \simeq 0.04$ eV, at normal conditions and the Maxwellian probability distribution of the energies

$$F(\epsilon) \propto \sqrt{\epsilon} e^{-(\epsilon/kT)}. \tag{10}$$

In the absence of other effects a localized distribution of charges diffuses by multiple collisions following a Gaussian law

$$\frac{dN}{N} = \frac{1}{\sqrt{4\pi Dt}} e^{-(x^2/4Dt)} dx, \tag{11}$$

where dN/N is the fraction of the charges found in the element dX at a distance x from the origin after a time t, while D denotes the diffusion coefficient which is a gas constant.

6.3.2 Drift of electrons with electric field

Due to their small mass, electrons can substantially increase their energy between collisions with the gas molecules under the influence of an electric field. The energy distribution will therefore change from the original Maxwellian shape and the average energy can exceed the thermal value by several orders of magnitude in high fields. The diffusion of the electrons is then perturbed by a superimposed directed drift motion and their distribution will change to

$$\frac{dN}{N} = \frac{1}{\sqrt{4\pi Dt}} \exp\left(-\frac{(x - tu_D)^2}{4Dt}\right) dx, \tag{12}$$

where u_D is the drift velocity of the electrons. The electrons are accelerated by the electric field, while at the same time they are decelerated by statistically distributed collisions with the gas molecules.

6.4 Gas amplification

In most of the region where the charges are produced by the primary interaction processes, the electric field only makes electrons drift towards the sense (anode) wires and positive ions towards the cathodes. But very close to the anode, normally at a few wire radii, the field gets strong enough so that multiplication starts. A typical drop-like avalanche develops with all electrons in the front and ions behind. If λ is the mean free path of an electron until the next ionization event, the reverse, $\alpha = 1/\lambda$, gives the probability of such an event per unit length. The value α is called *Townsend coefficient* which is a function of location.

If n is the number of electrons, we will have the creation of $dn = n\alpha(x)dx$ new electrons per unit length dx. Thus, the multiplication factor M is given by integration as

$$M = \frac{n}{n_0} = \exp\Big(\int_{r_1}^{r_2} \alpha(x)\Big)dx. \tag{13}$$

The multiplication factor cannot be increased arbitrarily. Secondary processes, like photon emissions inducing the generation of avalanches spread over the gas volume, and space-charge deformation of the electric field (which is strongly increased near the front of the avalanche), eventually result in a spark breakdown. A phenomenological limit for multiplication before breakdown is given by the Raether condition

$$ax \sim 20 \tag{14}$$

or $M \sim 10^8$; the statistical distribution of the energy of electrons and therefore of M in general does not allow one to operate at average energies above $\sim 10^6$ if one wants to avoid breakdowns. In the case of HADES, the factor M is around 2 - 3·10^5.

6.5 Choice of the gas filling

Since avalanche multiplication occurs in all gases, virtually any gas or gas mixture can be used in a drift chamber. In most cases, however, the specific experimental requirements – many times conflicting – restrict the choice to several families of compounds. Some of these requirements are low working voltage, high gain operation, high rate capabilities, long life time, fast recovery and so on.

Avalanche multiplication occurs in noble gases at much lower fields than in complex molecules; this is a consequence of the many non-ionizing energy

24

dissipation modes available in polyatomic molecules. Therefore, the convenience of operation suggests the use of a noble gas as the main component. Addition of other components will slightly increase the threshold voltage.

Polyatomic molecules have a very different behaviour, especially when they contain more than four atoms. The large amount of non-radiative excited states (rotational and vibrational) allows the absorption of photons in a wide energy range. This is a common property of most organic compounds in the hydrocarbon and alcohol families. The molecules dissipate the excess energy either by elastic collisions or by dissociation into simpler radicals. Even small amounts of a polyatomic quencher added to a noble gas changes completely the operation of a counter because of the lower ionization potential. Good photon absorption and suppression of the secondary emission allows gains in excess of 10^6 to be obtained before discharge.

6.6 Drift velocity

As mentioned before, a drift chamber is a detector which offers the possibility of measuring the electron drift time to get information about the spatial coordinates of an ionizing event. In its basic form, a single-cell drift chamber consists of a region of moderate electric field, followed by a proportional counter. Suitable field shaping electrodes, wires or strips, allow one to obtain the desired electrical configuration. Electrons produced at time t_0 by the incoming charged particle migrate along the electric field lines with velocity v and reach the high field region approximately 1 mm from the anode wire where avalanche multiplication starts at a time t_1. The coordinate of the track, with respect to the anode wire, is therefore given by

$$
x = \int_{t_0}^{t_1} v\, dt \, ,
\tag{15}
$$

which reduces to $x = (t_1 - t_0)v$ for a constant drift velocity. It is obviously very convenient to have a linear space-time relationship and this can be obtained in structures with uniform electric field. If a large surface of detection is required, a multi-cell structure can be used. In this case, the region of the anode wire becomes necessarily part of the active volume. So it is not possible to obtain a constant drift field everywhere across the cell, as the low field region between the anode wires would result in a strong non-linearity of the space-time relationship, especially for large wire spacings. A modification of the structure allows the elimination of low field regions between the anodes. The anode wires are alternated with five times thicker field-shaping cathode

wires that reinforce the electric field in the critical region, sharpening at the same time the transition from one cell to another.

7 The four planes of drift chambers

As already mentioned in previous sections, each plane of drift chambers consists of six trapezoidal modules shaped as a frustum. One module covers 60° of azimuthal angle. Module sizes range from 88 cm (large base) × 80 cm (height) (plane I), to 280 cm × 230 cm (plane IV). A chamber module is composed out of six drift cell layers oriented in five different stereo angles. These stereo angles (± 40°, ± 20°, ± 0°) have been chosen in order to enhance the precision of the kick angle measurement and reduce ambiguities. The cell sizes vary from 5 × 5 mm^2 to 14 × 10 mm^2 from plane I to IV to achieve a constant granularity, as already mentioned. Hence, the number of read-out channels per module, independent of its size, is constant (ca. 1100 cells).
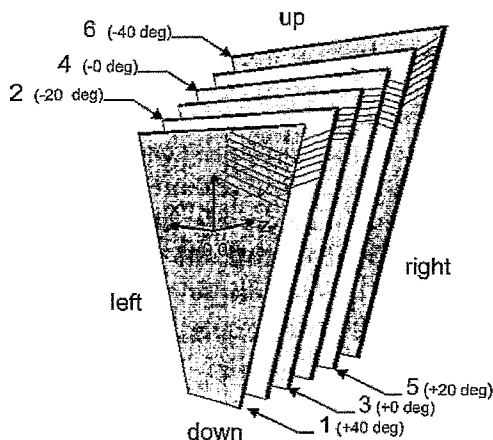

Figure 10: Schematic view of the anode frames inside a chamber module.

7.1 Construction of the third plane

The drift chambers constructed in the FZ Rossendorf form the second largest tracking plane of the spectrometer. Since they comprise the third plane, we use the abbreviation MDC III for them. They consist of six modules with an active area of roughly 2.2 m^2 for each plane and a drift cell size of 8 × 2 mm^2. Each module has six drift cell layers, i.e. six anodes and seven cathodes, consisting of wires glued on stesalith frames. The anode layers contain alternately sense wires (gold coated tungsten, $\varnothing = 20$ μm) and field wires (aluminium, $\varnothing = 100$ μm) with a distance of 6 mm from

each other. The wires in the six anode layers have five different orientations, as mentioned above (see Fig. 10), whereas the wires in the cathode layers (aluminium, $\varnothing = 80 \; \mu$m) always have the same orientation (+ 90°) and a distance of 3 mm.

The wire planes are prepared by using an automatic winding machine which has a high precision in the positioning (primarily $\pm$ 2 μm). This allows us to wind sense and field wires on one frame. Nevertheless, due to the big diameter of the field wires and their intrinsic tension, they roll away from their initial position. To correct this displacement for the case of anode layers, four combs have been installed at the two ends of the frame of the winding maschine. These combs help to improve the accuracy which reaches the ultimate value of $\pm$ 10 μm. To avoid any further dislocations a mechanical tension is applied during the winding process (0.5 N for the sense wires, 1.5 N for the field wires and 1.0 N for the cathodes). This tension also compensates for the deformation (sag) of the wires due to gravitational and electrostatic forces.

The wires are placed and glued with an isolating araldite glue on the stesalith frames. The process takes place in two stages because of the large size of the module. A special table, markers on the frames and cameras ensure that the wires are accurately placed, at the right distances (see Fig. 11) and on the same plane. For the field and cathode wires an additional conductive glue containing silver is used for the formation of the galvanic contact. The sense wires are soldered from one side on a printed circuit connector, whose other other side leads the invoked electric signal to the readout electronics via flex print cables (FPC).
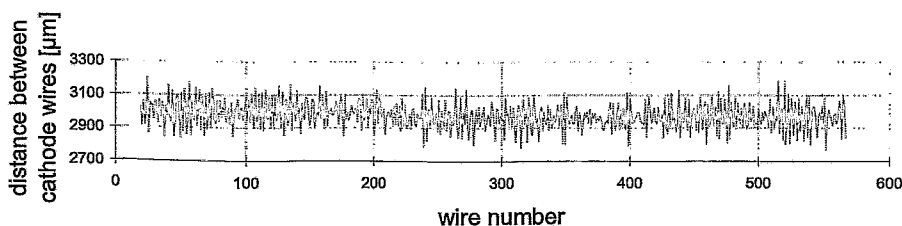

Figure 11: The measured position accuracy of the cathode wires for the second cathode plane of the first chamber has an error of $\pm$ 100 μm which is acceptable.

28

7.2 Mechanical tension measurement

The next task to be performed is the measurement of the streching force with a wire tension meter. A current pulse is fed into the measured wire, connected electrically to the instrument, deflecting it from its quiescent position perpendicuarly to a dipolar magnetic field (the deflecting force is produced by the interaction of the magnetic field of the current pulse with the magnet). The wire begins vibrating as a stretched string. Under the influence of the constant magnetic field, electric current is induced in the vibrating wire. The electric signal is amplified to a level necessary to drive the monostable multivibrator of the instrument at the suitable moment, providing another deflecting pulse. By appropriate regulation of the driving and deflecting signal, the wire starts vibrating continuously with nearly constant frequency.[4]
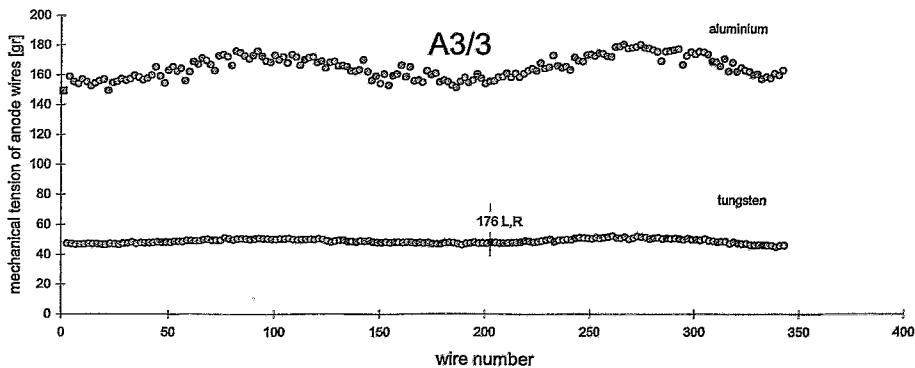

Figure 12: The measured wire tension of the field (Al, $\emptyset = 100$ μm) and the sense wires (W, $\emptyset = 20$ μm) in a zero degree frame of the third chamber. The unit of the force is in ponds, i. e. g on the earth surface.

In the case of a stretched wire with homogeneous cross section and density, with a diameter negligible compared to its length and vibrating with an amplitude negligibly small in comparison with the longitudinal dimensions, from the period T of the fundamental frequency the stretch F (in N) can be

---

[4]The development of various wire chambers since early 1970's and the task of manufacturing reliable, long-lived and high-quality instruments motivated many different approaches to measuring wire tensions. Usually, more indirect methods are employed in which the wire is first forced to vibrate, stimulated either by the Lorentz or the Coulomb force, and then these vibrations are used to determine the tension. A more detailed description of the available methods can be found in the following literature: [16], [17], [20], [21], [22], [23].
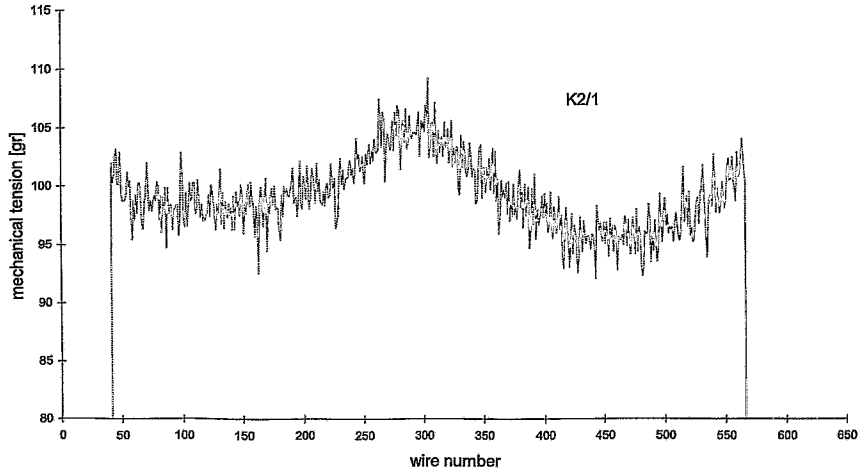
Figure 13: The measured wire tension for the case of the second cathode frame of the first chamber (Al, $\varnothing = 80~\mu$m).

determined by

$$F = 100 L^2 d^2 \rho \frac{\pi}{g} \frac{1}{T^2},\tag{16}$$

where L is the length of the wire in mm, d its diameter in μm, ρ the density in g/cm^3, T the measured period in ms and g the gravitional acceleration of earth (9.81 m/s^2). Applying the above method, one obtains the measurements shown in Figs. 12 and 13.

Although the wires are winded with a well defined constant tension, the measurement shows that this is not longer the case, when they are fixed on the frames. The stretching force of the wires consequently causes a deformation of the stesalith frames. The result is that the measured tension follows this deformation, as seen in the simulation of Fig. 14. The fluctuation is more evident for aluminium due to its smaller elasticity. The calculation was performed for a frame fixed on the table with four bolts in the middle of every side.

For one cathode layer the wire tension was measured twice; first, when the frame was placed on the special table where the wires are glued. In this case, apart from the four bolts, 29 additional holders were preventing the deformation. The measurement was repeated after the holders were removed

30

and the plane was lying in the tent only with the support of the four bolts. The results are illustrated in Fig. 15. A variation of the tension in the order of 20 % is not critical for the sag.
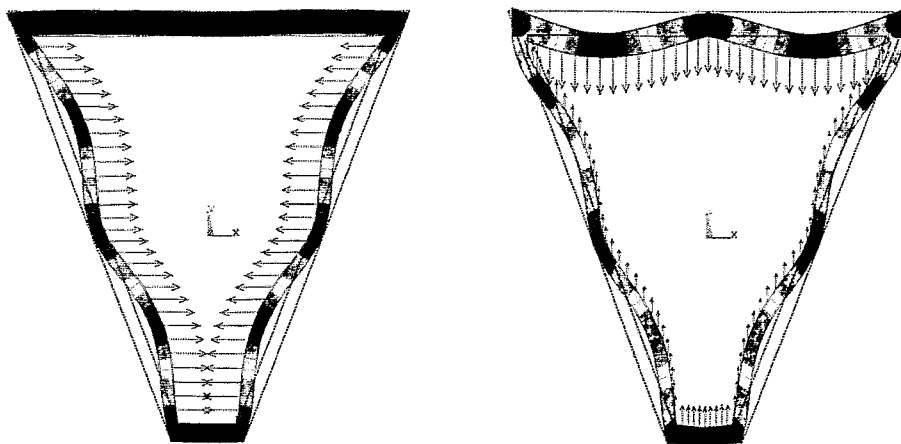

Figure 14: Simulations of the expected deformation of stesalith frames caused by wire tension. On the left side a 0° layer is depicted, while on the right it is shown that the deformation of a cathode is far more intense (see top and bottom parts of the frame) due to the large number of the wires.
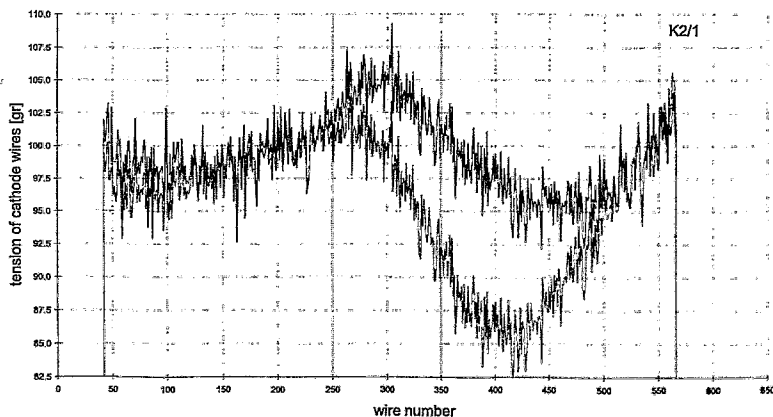

Figure 15: Tension of cathode wires. The upper curve is for the frame with the holders and the lower one for the frame with only four bolts. The measurement was performed for the second cathode frame of the first chamber.

31

7.2.1 Wire displacements due to gravitational and electrostatic forces

So far we have considered the wires on the stesalith frames without taking into account the behaviour of the tension under working conditions. Apart from the gravitational forces which are always present, the wires are also subject to electrostatic forces that tend to displace them, when voltage is applied. The combined effect of these forces and of the restoring mechanical tension results in an elastic deformation of the wire. The wire deflection from the nominal position can be estimated by solving the differential equation which describes its equilibrium state. Such a calculation can be performed with the programme Garfield (see Ch. 8). The differential equation describing the shape $y(x)$ of a wire (x runs along its length) subjected to an external force $f(x)$ can be derived by making the following assumptions:

- the wire deflection is small compared to the length of the wire

- the wire elongation is in the elastic range of the Hooke's law.

If the wire is stretched under tension T and has a shape $y(x)$, the force F_t acting on an elementary part of the wire between x and dx is given by:

$$F_t(x)dx = T(\frac{dy}{dx})_{x+dx} - T(\frac{dy}{dx})_x = T\frac{d^2y}{dx^2}dx \qquad (17)$$

This is the force that tends to restore the wire back to its nominal position and balances any external applied force. The gravitational force per unit length acting on the wire is $F = g\rho\sigma$, where ρ is the density of the wire and σ its cross section, while the electrostatic force is $F = \lambda E$, where λ is the charge per unit length and E the electric field generated by the surrounding electrodes. If the field is constant, it creates a constant force per unit length, similar to the gravitational one. For a wire placed in a position of electrostatic equilibrium, a small deviation from this position generates a force acting on the wire tending to displace it. This force has the form $F = \dfrac{V^2}{2}\dfrac{dC}{dx}$, where V is the potential of the wire and dC/dx the variation of its capacitance per unit length due to displacement. It can be shown that

$$F \simeq \frac{V^2}{2} \frac{4\pi\epsilon_0}{[\alpha ln(\alpha/r)]^2}x = ky, \qquad (18)$$

where r is the radius of the wire and α the typical distance of the wire from the other electrodes.

Thus, the equation describing the equilibrium position of the wire is

$$T\frac{d^2y}{dx^2} = -ky - g\rho\sigma = f(x). \tag{19}$$

For $k = 0$ we can study separately the effect of gravity. In this case the sagitta of the wire is

$$s_g = \frac{L^2 g\rho\sigma}{8T} \tag{20}$$

and is proportional to the inverse of the mechanical tension T. If T is increased, the effect is reduced but it cannot be arbitrarily increased, since non-elastic deformations take place. The total sagitta of the wire under the combined effect of electrostatic and gravitational forces is

$$s = \frac{8s_g T}{L^2 k}\left(\frac{1}{cos\sqrt{k/T}(L/2)} - 1\right) = s_g\frac{2}{q^2}\left(\frac{1}{cosq} - 1\right). \tag{21}$$

It is clear that the electrostatic forces amplify the sagitta produced by the gravitational forces. From the above equation we can deduce the stability condition

$$q^2 = \frac{4\pi\epsilon_0}{[\alpha ln(\alpha/r)]^2}\frac{V^2}{2T}\frac{L^2}{4} \le 1. \tag{22}$$

Using the above inequality, it is possible to calculate the critical tension T_c, below which the wires oscillate under working conditions. Choosing, for example, $\alpha = 4$ mm, $L = 2$ m and $V = 2000$ V, we get $T_c = 0.31$ N for sense (r = 10 μm), $T_c = 0.65$ N for cathode (r = 40 μm) and $T_c = 0.72$ N for field wires (r = 50 μm).

7.2.2 Calculation of wire sagittas

Whether the solution of the above differential equation (Eq. 19) is exact or not depends on the shape of $f(x)$. If it is chosen to have a linear or second order dependence from $y(x)$, exact solutions can still be found. For higher order terms though, numerical methods are needed to compute the wire shape. Such a method consists of the following steps:

- Select the sample points and compute the sag and its first derivative for the linear force.

- Prepare an interpolation table of the force for various shifts.

- Use the 5th order Runge-Kutta-Nyström stepping method for calculating a solution between the sampling points.

- Perform the Newton-Raphson zero search to minimize the difference between the solution on the left and the right side of the sampling points, as well as the difference between the first derivatives at the same points (see Fig. 16, 17).
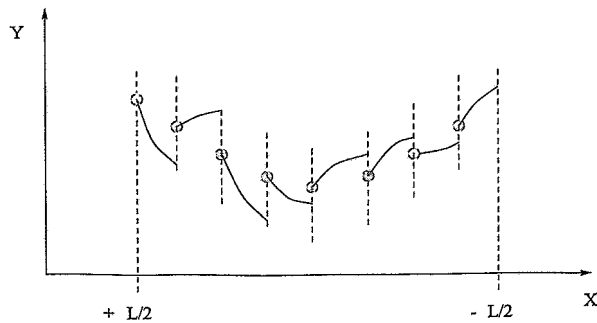

Figure 16: Extrapolation of the solution using a stepping method between the sampling points.
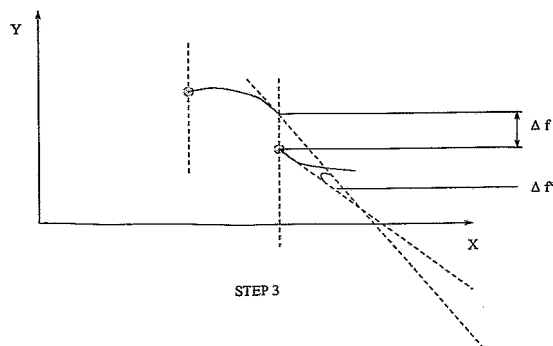

Figure 17: Zero search of Δf and $\Delta f'$.

7.2.3 Examination of the wire deflections for the MDC III

Following the above we attempted to calculate the sagittas for the wires of MDC III as a function of their tension, without varying the potential applied

on field and cathodes. There might be that the wires lose tension by creeping out of the araldite glue on the stesalith frame. In case a wire is loose enough to affect the resolution of the chamber - this applies to sense wires, it is possible to make corrections by knowing the size of the deflection along the wire.

The calculation was performed for a series of tension values between the strung and the critical one and for different layers and chamber orientations. The results for $V_c = V_f = -2000$ V are depicted in Figs. 18, 19, 20. The plots show that sense and field wires of the $0°$ layer are subject to the highest deflection from the nominal position. The situation is better for inclined layers and chambers. Nevertheless, for a loss of 20% in tension, the sag is not higher than the resolution of the modules (100 μm), e.g. for 0.4 N (40 g) the sag of $0°$ layer in sector 1 is below 80 μm.
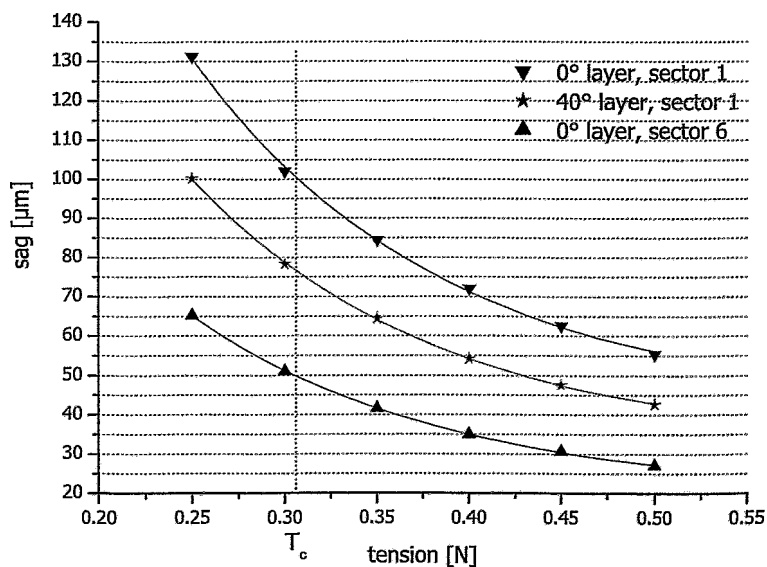

Figure 18: Deflection of sense wires as a function of their tension. For the nominal tension of 0.5 N the calculated sag is far below the resolution of the chambers.
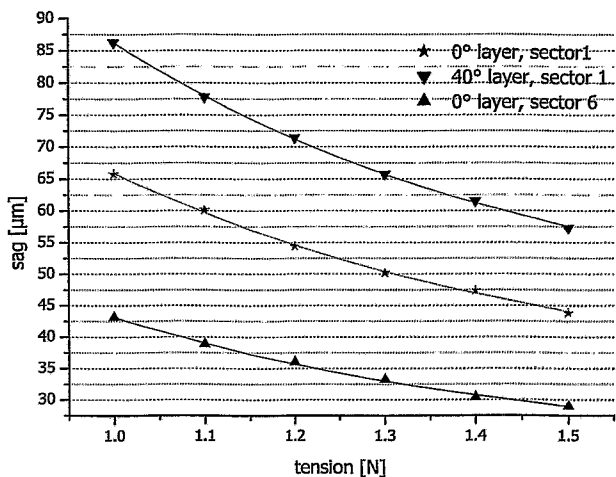
Figure 19: Deflection of field wires as a function of their tension. As in the previous figure, the nominal tension assures that the deflection is not of great importance and does not influence dramatically the resolution of the detector.
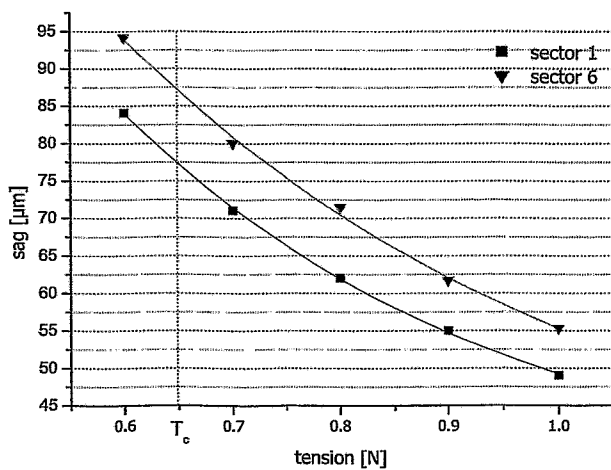

Figure 20: Deflection of cathode wires as a function of their tension.

7.2.4 Method for the separation of wires in faulty contact

The stable operation of an MDC module requires constant high voltage on the field and cathode layers. Yet, during the operation, it might be the case that there is a persistent local discharge around a cathode (field) wire C_i (F_i) which can lead to an instant drop of its potential. This abrupt change will lead to an attractive force between wires of sequential layers and quite often to a spark which can provide sufficient energy for the wires to weld.

The origin of this phenomenon was studied using two (dummy) layers of wires at a distance of 4 mm, on which both kinds of electrodes (field wires, $\varnothing = 100$ μm; cathode wires, $\varnothing = 80$ μm) were strung with the operational tension, i. e. 1.5 N and 1.0 N respectively. The sense wires were not included in the study. With this setup it was proven that a rise of the potential above a certain value may cause wire oscillations and sparks and moreover, even recreate a faulty connection between the layers. Here we have to point out that in the case of the dummy frames, what we have is rather a superficial attachment than welded wires, meaning that a mechanical vibration is often sufficient to cure the faulty connection. No external damage on the surface of the wire was observed.

From high-frequency engineering it is known that spark-over paths can be repaired with the help of high voltage pulsers. This method would be suitable for the repair of the faulty connection in our case. Furthermore, a short current pulse can induce a force on the wire. When we deal with such
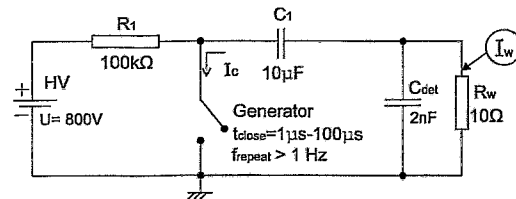

Figure 21: Time controlled high voltage switcher.

a case in a chamber installed in the HADES setup, it is always practical and less time consuming to repair the chamber without removing and opening it. Using the above dummy frames, such a method for repairing the faulty connection of the wires was tested. The fundamental idea was to use a time controlled switcher for a pulse source (Fig. 21). Keeping the switch closed, the charged capacitor discharges on the connection of the two Al wires through the resistivity $R_w \sim 10$ Ω. The simulated discharge current for the time constant of $\tau = R_w C_1 \simeq 100$ μs is depicted in Fig. 22. For flexibility purposes

a generator is used in order to vary the duration time t_{close} and the pulse repetition rate f_{repeat}. Experience showed that a duration of $t_{close} = 10$ μs
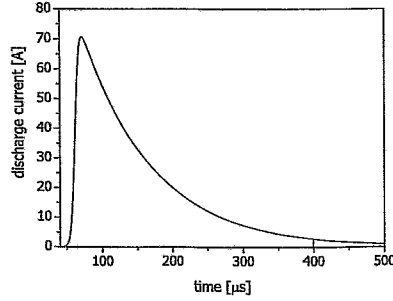
Figure 22: Plot of the simulated discharge current as a function of time.
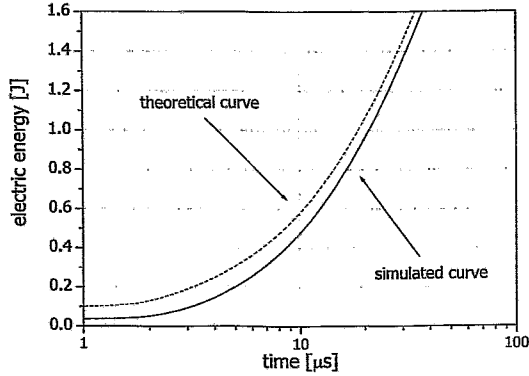
Figure 23: Overlay of theoretical and simulated curve of the dissipated electric energy as a function of time.

and frequencies f_{repeat} higher than 1 Hz are appropriate. A glow lamp (not shown in the circuit) signalizes the successful separation of the wires. The electric energy (Fig. 23) for the above circuit was simulated with PSpice [18] and was calculated from the time integral of the electric power as

$$W = \int_0^{t_{close}} U_w I_w dt. \tag{23}$$

38

For $t_{close} = 10$ μs and $U = 800$ V the dissipated energy is $W \simeq 0.5$ J while the theoretical curve, also calculated by integration, gives $E = 0.6$ J. In contrast to the direct heating method [19] which induces energies of about 25 J on the wire connection, the short energy pulses provide safety against smelting wires.

7.3 Gas and high voltage tests and efficiency estimation

After measuring the mechanical tension, the frames are put together and the detector is covered from both sides by two mylar windows (12 μm thickness), coated internally with aluminium (120 mg/m^2). The thin aluminium layer serves as protection against the charges that might gather on the foil, perturbing locally the electric field and thus affecting the normal operation of the chamber. Between the frames, rubber (viton) ensures the gas tightness of the chamber. Three stiffeners screwed on the three big sides of the module restore any deformation of the frames.

In order to test the gas tightness, the detector is filled with nitrogen and sealed. A thread stretched along the mylar helps measuring the loss of the gas by comparing the different heights of the foil, as a function of time.

Assuming for the purpose of an estimate a spherical geometry (see Fig. 24), the volume of half of the detector will be
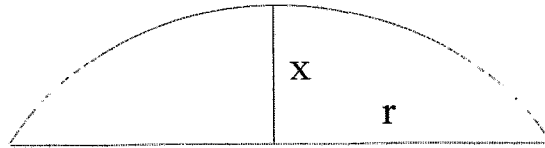
Figure 24: Cross section of the assumed spherical geometry.

$$V = \frac{1}{6}\pi x(3r^2 + x^2) \Rightarrow V = \frac{1}{6}\pi x \cdot 3r^2\Big(1 + \frac{x^2}{3r^2}\Big). \tag{24}$$

Knowing that $A = \pi r^2$, the above equation becomes

$$V = \frac{1}{6}\pi x \cdot 3\frac{A}{\pi}\Big(1 + \frac{x^2\pi}{3A}\Big) \approx \frac{1}{2}A \cdot x, \tag{25}$$

where the term $\dfrac{x^2\pi}{3A}$ is almost zero and therefore omitted. If A_U is the spherical surface for the upper half of the detector and A_L the surface for the lower part of it, then the total volume is given by

$$V_{tot} = V_U + V_L. \tag{26}$$

In our case $A_U = 2.123$ m^2 and $A_L = 2.267$ m^2. Thus, assuming for instance that $x = 0.01$ m, the total volume will be $V_{tot} = 21.96$ l. The gas leakage

within the spherical geometry approximation is overestimated by about 30% but this is not of great importance due to the very low leakage rate of the chambers of 450 ml/h, exhibited in Fig. 25. The selection of nitrogen for this measurement also ensures that the heavier isobutane molecules will have an even lower leakage rate. A comparison with the leakage rate of helium shows that the difference in the two rates is not crucial (520 ml/h for He and 370 ml/h for N_2).
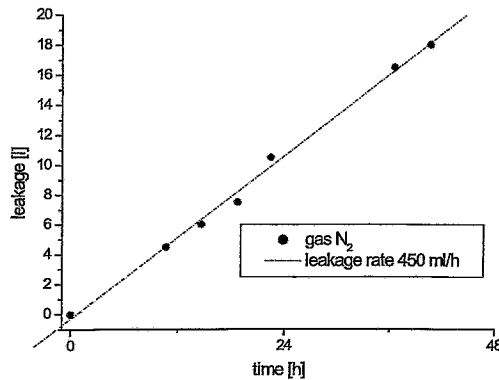

Figure 25: Gas leakage rate for chamber 3.

By applying high voltage on the field and cathode wires, it is ensured that the impedance of the planes is high enough (above 100 GΩ). The plot of the flowing current vs. applied voltage can provide us with the current characteristics of the chamber, i.e. the voltage which the avalanche multiplication starts for. Such a plot is depicted in Fig. 26. It is evident that for a covered chamber without presence of any external light or radiation source, the avalanche multiplication will start at around -2400 V. A similar curve is obtained with the presence of a ^{90}Sr electron source (50 kBq). A dramatic difference is observed in case of illumination from a nearby lamp. The avalanches appear at a much lower voltage (-2000 V). Photons of this frequency can extract electrons from the aluminium wires which act like photocathodes.

Before testing the electronics, it is necessary to confirm that all FPCs can deliver signals. Thus, a current pulse is fed into the field wires (transmitters), while the sense wires behave like receivers. The FPCs are connected to a preamplifier and the output signal is viewed with the help of an oscilloscope. Adjusting the characteristics of the pulse (duration, amplitude, etc.) in order
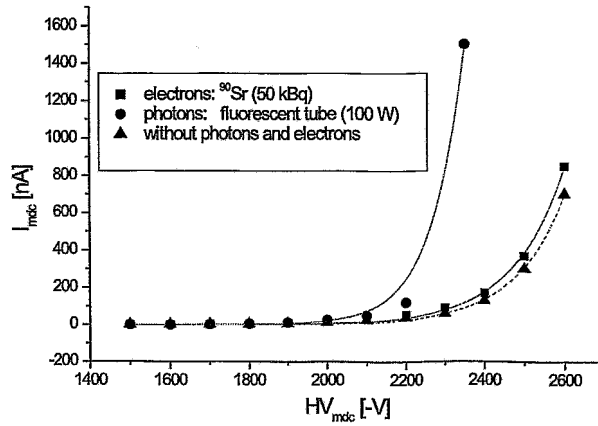
41

Figure 26: Current characteristics of the chamber 1.

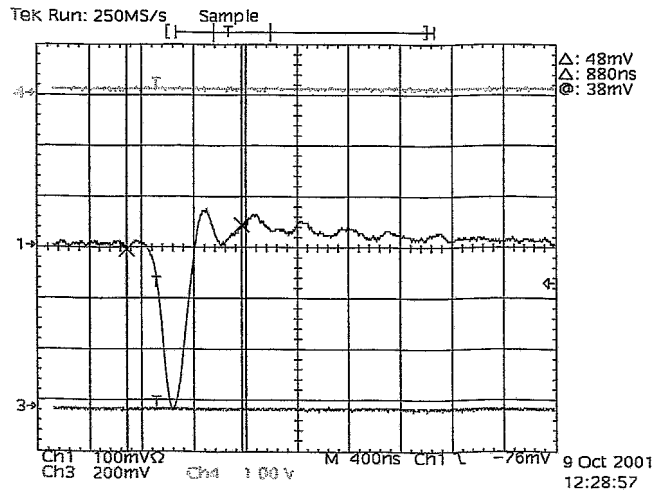to avoid reflections, the signal looks like that displayed in Fig. 27.

Figure 27: Analogue output signal of an anode wire from chamber 4 as seen with the oscilloscope.

It is also possible to make a first estimate of the counter efficiency of the individual planes of the detector. For this purpose two scintillating counters

42

are placed above and below the drift chamber. The schematic layout for this test configuration is displayed in Fig. 28. The ^{90}Sr source, lying on one of them, provides sufficient electrons to produce a detectable signal. The signals of the scintillators are lead to a coincidence unit in order to build the double coincidence R_2. The signals from the eight wires pass through preamplifiers and then an octal discriminator to deliver standard NIM (Nuclear Instrumentation Methods) signals. Afterwards they are logically added and their sum is sent to a second coincidence unit together with the signal from the first one. Thus, a triple coincidence R_3 is made (see Fig. 29).
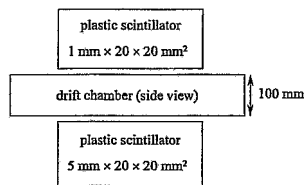
Figure 28: Experimental setup for efficiency measurement.
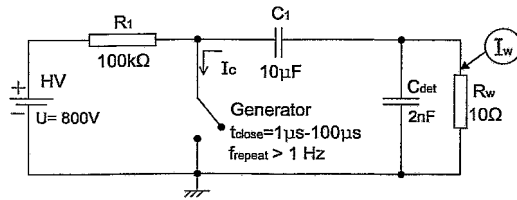
Figure 29: Circuit for realizing the efficiency measurement. The eight arrows on the upper left side represent the signals from the anode wires.

The efficiency ϵ is defined as

$$\epsilon = \frac{R_3}{R_2},\tag{27}$$

where R_2 and R_3 are the counter rates corresponding respectively to the number of double and triple coincidences. The plot of the efficiency as a function of high voltage is depicted in Fig. 30. The plateau is the area where the avalanche multiplication is the dominant process and the area where the chamber is operated. The errors are estimated by the assumption that the double coincidences are not independent from the triple ones. Thus,

$$\epsilon = \frac{R_3}{R_2} \pm \frac{\sigma}{R_2}.\tag{28}$$

43

Supposing that the number of particles crossing the detectors follow a binomial distribution, the standard deviation of R_3 will be $\sigma(R_3) = \sqrt{R_2 \epsilon (1 - \epsilon)}$. Inserting ϵ from Eq. 25,

$$
\begin{aligned}
\sigma(R_3) &= \sqrt{R_2 \frac{R_3}{R_2}\left(1 - \frac{R_3}{R_2}\right)} \\
&= \sqrt{R_3\left(1 - \frac{R_3}{R_2}\right)} \Rightarrow \\
\epsilon &= \frac{R_3}{R_2} \pm \frac{\sqrt{R_3(1 - R_3/R_2)}}{R_2}.
\end{aligned} \tag{29}
$$
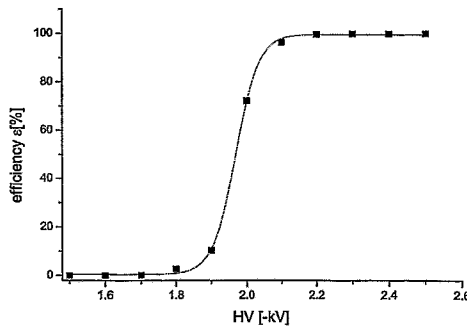
Figure 30: Efficiency of the two middle layers of the drift chamber 3 with respect to the applied voltage. The calculated error bars are very small and thus not visible.

The efficiency depends not only on the applied voltage but also on the gain of the preamplifier and its threshold. Usually for voltages larger than -1900 V the electrons obtain sufficient energy to reach the sense wires producing avalanches on their way. Thus, the efficiency curve reaches its characteristic plateau very close to 100 %. This is the region where the drift chamber is operated.

The dependence of the efficiency with respect to the layer can be studied, if the same efficiency plot is produced for all the layers. It appears that the $\pm 20°$ and $\pm 40°$ layers reach the value of 50 % for a higher voltage. This dependence is depicted in Fig. 31. The difference can be explained by the fact that the potential close to the mylar foils has a different distribution from the one in the centre where the 0° planes are located.

44

Figure 31: Dependence of the efficiency with respect to the wire orientation of the layers (chamber 1).

7.4 Concept of the readout

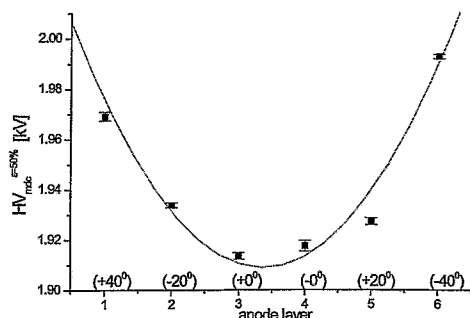On the frame around the detector the installed Front-End-Electronics (FEE) serve the readout of the signal produced by the charged particles in the active volume of the detector. The chambers are equipped with dedicated 16-channel preamplifier/shaper/discriminator (ASD-8 chip) boards (daughterboards) inserted into motherboards (64 or 96 channels) which themselves contain the digitizers (Time to Digital Converters (TDC), 8 channels).

The daughterboards routinely deliver a logical (differential) signal which measures the time of the amplified analogue pulse above an adjustable threshold. Each one of them simultaneously amplifies the signals of eight sense wires and produces subsequently a pulse. A threshold discriminator will generate start signals. The TDCs in combination with an outer common stop signal, digitize without dead time the time difference between the start and stop signals. Fig. 32 schematically explains the procedure.

The chip of the motherboards measures up to two times per read-out cycle, depending on the chosen mode:

- Leading and trailing edge of the logical ASD-8 signal: the resulting time difference is called "time-above-threshold" and can be used to discriminate spikes and pile-ups. This mode is commonly used.

- Two leading edges: in large drift cells (e. g. long drift times) of the outer chambers two hits in one event can be resolved. This mode has not yet been used during the test experiments.

45
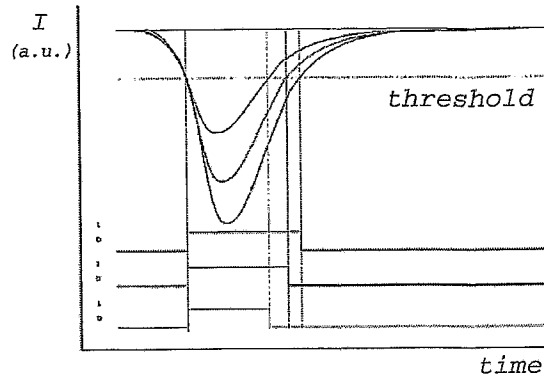
Figure 32: Digital pulses produced for various thresholds. A typical scale for the produced pulse is 100 ns.
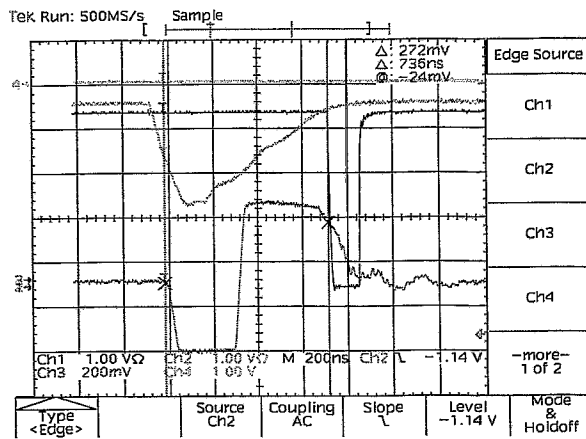
Figure 33: On the top of the figure depicted are the analogue signal from a daughterboard and the common stop signal by the generator. On the bottom we see the output of the daughterboard after the digitization.

In order to ensure that the FEE work properly without triggering on noise, after their installation on the chamber a test with a PCI (Personal Computer Interface) card has to be carried out. In this test the stop signals are created by a pulse generator. The PCI card reads the output of the TDCs and delivers the time difference between the two signals. An example of a digitized signal coming out of the TDC is illustrated in Fig. 33.

8 Simulations of electric field in drift chambers

As mentioned above, the purpose for the use of drift chambers is that they provide us with the possibility to define the trajectory of a charged particle which has crossed the detector. This is done indirectly by using the arrival time information and the drift velocity of the produced electrons in the gas medium of the chamber. The general formula for the calculation of the distance between the production place of the first electrons until the sense wire is given by Eq. 15. Although it is very convenient to have a linear distance-time relationship, this is not always possible due to the geometry of the chamber which leads to field irregularities. In order to find the optimum potential configuration that will provide a simple relationship, simulations with two- and three-dimensional programs were performed. In the present report, the results of these simulation codes are presented.

8.1 Simulations of electric fields using GARFIELD

GARFIELD is a computer program for the detailed simulation of 2-dimensional drift chambers with which different geometries and detector properties can be studied. The program gives the user the possibility to apply electric potentials on the wires and then to calculate the electric field with a precision of 10^{-8}. The user is also given the possibility to set trajectories of charged particles from which GARFIELD drifts electrons calculating their arrival time distributions and distance-drift time relations.

Another interesting and useful feature of GARFIELD is the interface with Magboltz. Magboltz allows the definition of various gas parameters for different gas mixtures up to four gas components. The equation that needs to be solved to provide the above information is the Boltzmann transport equation

$$\frac{\partial(nf)}{\partial t} + \vec{v}\frac{\partial(nf)}{\partial \vec{r}} + \frac{e\vec{F}}{m}\frac{\partial(nf)}{\partial \vec{v}} = B(t). \tag{30}$$

It describes the temporal and spectral changes of the electron phase space distribution $f(\vec{v}, \vec{r}, t)$. $n = n(\vec{r}, t)$ is the density of the free electrons in the gas medium, $\vec{v}$ their velocity, $\vec{F}$ is the outer force that acts on the electrons ($\vec{F} = e\vec{E}$ in case of an electric field) and m is the electron mass. $B(t)$ is the so-called collision term which contains the distribution function of the impact partner. So, the Boltzmann transport equation describes the drift and diffusion of electrons in gases under the influence of electric and magnetic

fields. The calculations are based upon previously measured input parameters, such as cross sections for elastic and inelastic scattering of electrons in gas. Output parameters can be the drift velocity, the diffusion coefficient and the Lorentz angle (for given electric and magnetic field, as well as known gas temperature and pressure).

8.2   The geometry of the drift chambers in GARIELD

GARFIELD is originally limited to two-dimensional chambers consisting of wires and planes, since analytical solutions for three-dimensional configurations, even simple ones, are not known. Because of this fact, the exact representation of crossed wires geometry is not possible. Instead, the cathode planes have to be replaced by wires which are parallel to the anode and field ones. The limitations of the program do not permit the simulation of the $\pm$ 20° and $\pm$ 40° layers either. Thus, the two middle layers of the detector will look as depicted in Fig. 34. The cathode planes are represented by a sequence of wires placed at a distance of 1 mm in parallel to the sense and field wires which are placed at the real distances.

```
:*********************************
    o      *     o      *      c      *
:*********************************
    *      o      *      ⊃      *      ◠
:************************************
```
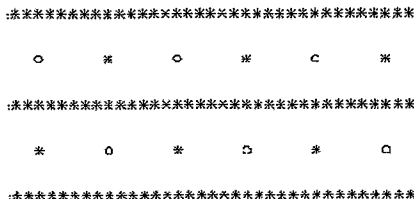
Figure 34: The geometry of the drift chambers in GARFIELD. The cathode and field wires are labelled as starlets * while the sense wires are represented by circles o.

For the selection of the optimum working voltage of the detectors, it is necessary to study the behaviour of the electron drift velocity in the given gas mixture. The high voltage for which this velocity reaches a plateau is the region where the chambers are operated. Indeed this region starts around $2 \cdot 10^3$ V/cm (see Fig. 35) and expands up to 10^4 V/cm. For different cell sizes, though, different voltages should be applied. This is the starting point for the GARFIELD simulations. Two field configurations for different applied high voltages are illustrated in Figs. 37 and 39. As expected, the field gradient around the thin sense wires is larger than around the thicker field wires, since

Figure 35: Drift velocity vs. electric field.

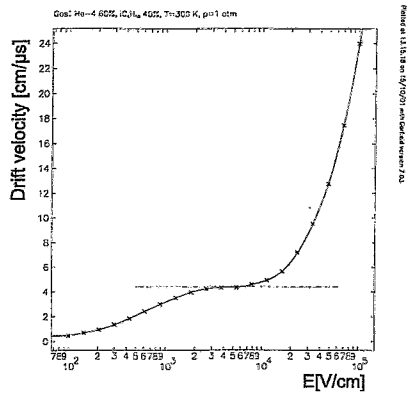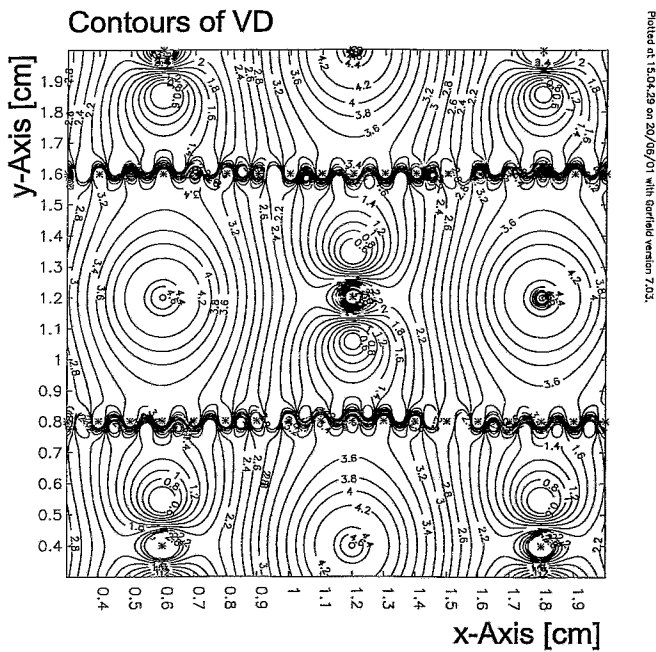Figure 36: Contour plot of electron drift velocity inside the drift cells for $V_c = V_f = -2000$ V.

$E \sim \dfrac{1}{r}$. In order to study the behaviour of the electron drift velocity inside such a field configuration, a contour map of the drift times can be helpful.

49

An example is exhibited in Fig. 36. It is clear that the electrons on their way to the sense wires intersect different drift velocity contours.
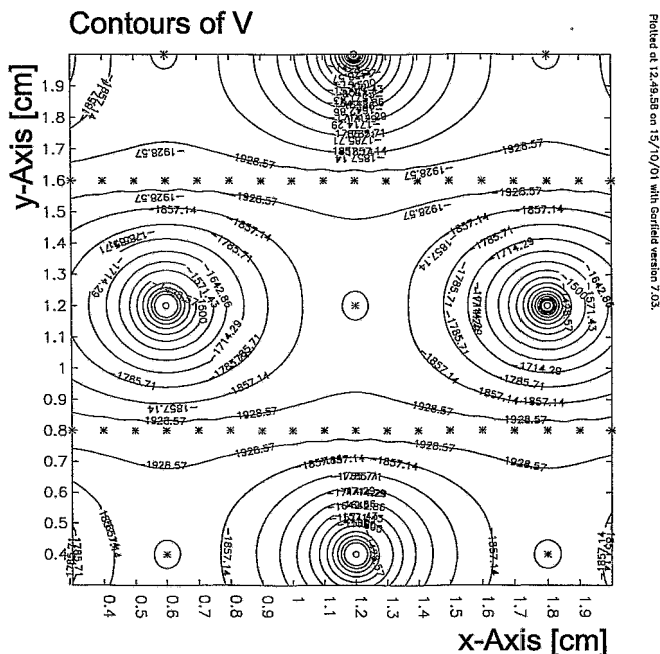
Figure 37: Contours of potential distribution for $V_c = V_f = $ -2000 V.

The fact that the cell is not square leads to the assumption that a higher potential on the field wires might compensate for this asymmetry of the cell dimensions. There is a limitation due to the multiplication factor M though. The absolute value should not exceed a certain level, so as to avoid the breakdown of the chambers due to sparking. To test this assumption, different potentials can be applied on the field wires, starting from -2000 V up to -2400 V with steps of 100 V.

The distribution of the isochrones directly evidences the linearity of the forementioned distance-time relationship. If the time contours are not homocentric with integer radii ratios, this implies the existence of non-linearity. This is actually the case for -2000 V (see Fig. 38).

By applying higher voltages on the field wires, a linear distance-time relationship is achieved, at least for a larger part of the drift cell. This can be seen in Fig. 40 for the case of -2400 V on the field wires. Nevertheless, despite of the fact that a larger area of the drift cell with constant drift velocity is obtained, there are regions at the border of the cells, where the

50
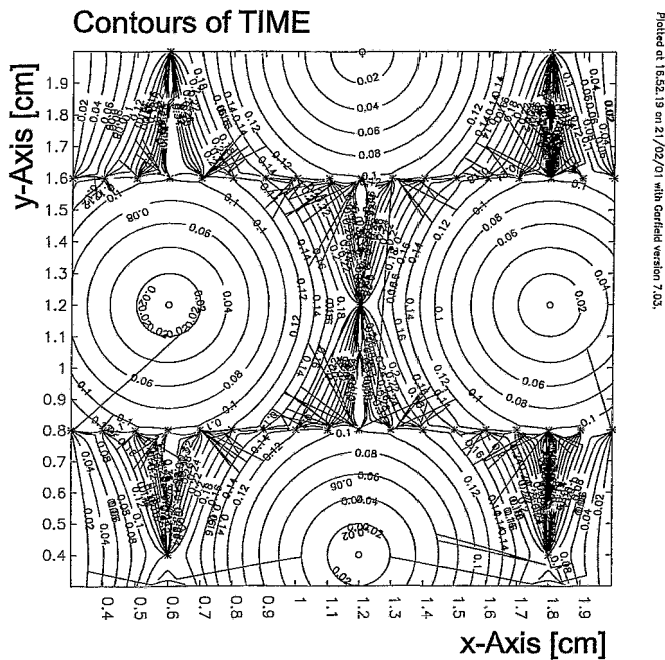
Figure 38: Contours of time for $V_c = V_f = $ -2000 V.

drift velocity is not constant. It is not clear enough which drift lines the produced electrons follow in these areas. The geometry in GARFIELD is also limited as far as the particle trajectories are concerned. That is, unless a three-dimensional field map is used. Such a map can be produced with one of the commercially available fine element programs.
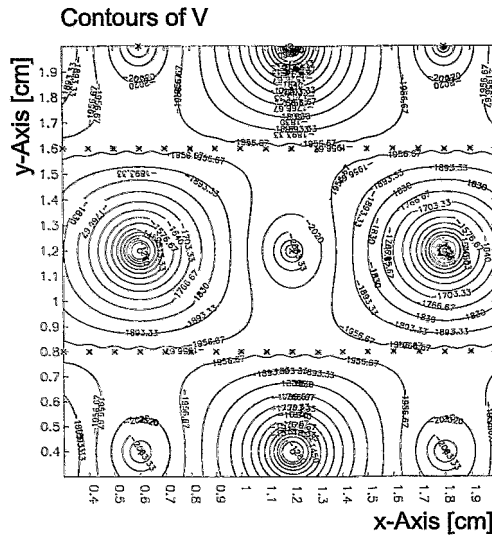
Figure 39: Contours of V for $V_c = -2000$ V and $V_f = -2400$ V. The drift cells are more clearly "visible", if the difference between the two values is larger.
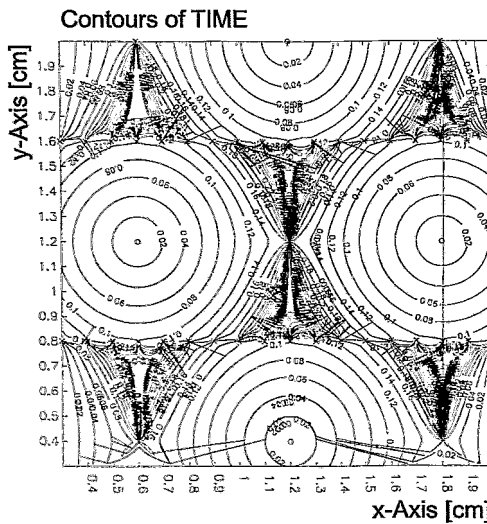
Figure 40: Contours of time for $V_c = -2000$ V and $V_f = -2400$ V. With this potential configuration the isochrones appear to be more homocentric with equal spaces between them.

8.3 Simulations with OPERA

Although GARFIELD was originally limited to two-dimensional chambers, it currently accepts two- and three-dimensional field maps computed by finite element programs such as OPERA, as basis for its calculations. The idea is to use the field map created by OPERA in combination with GARFIELD, so as to calculate the drift properties of the electrons in three dimensions. OPERA gives the user the opportunity to design the desired geometry, apply the potential and then solve the Poisson equation. The accuracy of the solution in such programs depends on the density of the mesh discretisation, as well as the boundary conditions applied. Symmetry also plays an important role and it should be used wherever it is possible.

Figure 41: Visible are two cathode planes, each one containing two cathode wires, as well as an anode plane with a sequence of alternating sense (thin) and field wires (thick). The crossed wire geometry of the drift chambers is now correctly represented. The position of the wires is accurate, while their shape is only an approximation.

The first attempt in our case was to simulate one of the middle drift layers of the chamber, i.e. an anode plane and two cathode planes. The cross section of the sense and field wires is hexagonal, while the cross section

of the cathode wires is quadratic. The "radius" of the sense and field wires equals the real one but in the case of the cathodes the perimeter of the wires equals that of the cylindrical ones. The created mesh is quadrilateral which gives a more accurate solution in less time. The three-dimensional geometry of the cell as well as a solution depicting the potential contours are given in Figs. 41 and 42.
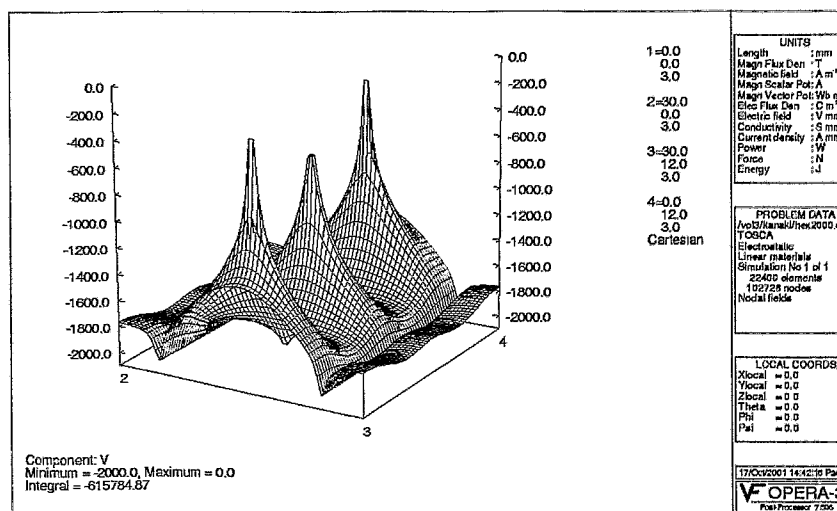

Figure 42: View of the potential distribution for $V_c = V_f = -2000$ V. The peaks represent the anode wires, while the two "valleys" are the cathode wires. Between the anode wires there are also two field wires.

8.4   Comparison of OPERA with GARIELD

Taking into consideration that the solutions provided by fine element programs are not analytical, a comparison between OPERA and GARFIELD would give us a measure of how reliable OPERA is, as far as the calculation of the field map is concerned. For this purpose a simple geometry is selected; a sequence of field and sense wires between two cathode planes. In GARFIELD infinite length along the z-axis and infinite periodicity along the x-axis are assumed (see Fig. 43). In OPERA this is not the case; the size of such a simulation is definite and restricted to a few wires.
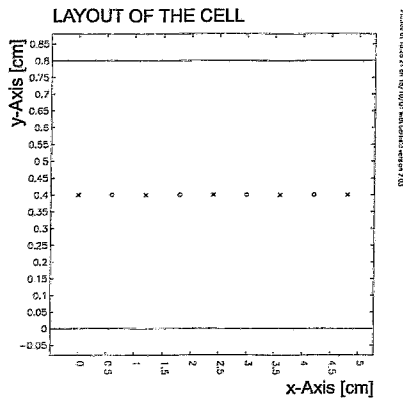
54

Figure 43: Scheme of wire positions for a comparison of GARFIELD simulations with OPERA. The sequence of cathode wires has been replaced by two planes (depicted as horizontal lines) with the same potential ($V_c = V_f = -2000$ V).
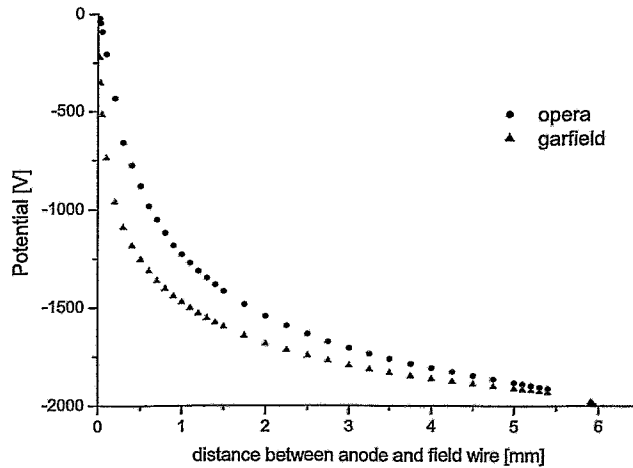

Figure 44: Plot of the potential distribution between an anode and a field wire. Very close to the surface of the anode wire GARFIELD provides the correct solution with an infinite field gradient, while OPERA gives a finite value.

Plotting the potential between an anode and a field wire over their distance, as in Fig. 44, it is evident that OPERA overestimates the correct solution. It can be considered satisfactory for distances larger than 1 mm from the anode wire. Actually, this is not a major problem in our case, since we are mostly interested in the drift properties of the electrons at the borders of the cells. In these regions the results by both programs fulfil our requirements.

9   Summary and conclusions

The present report was aimed at investigating suitable operational conditions for the drift chambers MDC III installed in the HADES setup. After a brief introduction into the physics motivation of the HADES project and the technical design of the detector, various simulations of the electric field configurations and corresponding drift velocities inside the drift cells were described.

The simulations performed with the code GARFIELD show that an increase of the voltage applied on the field wires with respect to the cathodes could lead to the wanted constant electron drift velocity over a larger area of the cell rather than by using the same voltage on all wires. This offers a simple way to compensate for the asymmetric dimensions of the drift cell. We propose to study this prediction comprehensively, using the calculated potentials.

Regarding the simulations, further steps have to be made in order to study the behaviour of the electron drift velocity in three dimensions. These steps should include the incorporation of OPERA field maps in GARFIELD and a more realistic comparison between the 2d- and 3d-simulations.

Operating the drift chambers in a mode with nearly constant electron drift velocity in a major part of the cell allows a more precise and fast tracking. This is particularly important for electrons and positrons; here the invariant dilepton mass must be reconstructed with high precision to get a resolution of $\Delta M/M \approx 1\%$ for the ω and ϕ mass peaks. This will allow to verify even small in-medium mass shifts; this helps to realize the physics program at HADES which focuses on the search for such mass shifts to get insight into the in-medium behaviour of hadrons in dense strongly interacting matter.

A Models for the description of heavy-ion collisions

The theoretical models used nowadays to study relativistic heavy-ion collisions can be roughly divided into two groups: **macroscopic** models based on nuclear fluid dynamics and **microscopic** models based on kinetic transport theory.

Macroscopic models describe the nuclear interactions by using hydrodynamic equations and assume local equilibrium. These models are mainly applicable for central collisions of heavy nuclei where the system has many degrees of freedom and the mean free path of the nucleons is short compared to the spatial dimension and gradients of the system. The great advantage of these models is that basic nuclear matter features, e.g. EOS supplemented by dissipative effects (viscosity, thermoconductivity) are used directly as input. However, relativistic heavy-ion collisions involve many quantum and non-equilibrium effects, particle production, fragment formation etc., and a more detailed description of these phenomena in relativistic heavy-ion collisions can be obtained by microscopic dynamics.

A microscopic dynamics description of heavy-ion collisions is usually based on transport theory. Here the propagation of individual particles is simulated. The main ingredients in this description are the cross sections, the two–body potentials and decay widths. Since the particles propagate in hot and dense matter, their properties might change significantly. Consequently, properties like effective masses, effective momenta, in-medium cross sections and decay widths should be calculated for the actual local situation in which the particle propagates. Furthermore, heavy-ion collisions demonstrate different features at different energies. At low energies, because of Pauli blocking of two body-collisions, a suitable approach is the mean-field theory, such as the time-dependent Hartree-Fock theory. At higher energies, the reaction dynamics at the initial stage is mainly governed by two-body collisions and particle production becomes increasingly important. For this purpose, various models have been developed which address specific features of selected energies. Some of these models of relevance for SIS energies are described below.

A.1 BUU-type models

At energies in the 1 GeV range and for the expansion stage of relativistic heavy-ion collisions, the effects of mean-field, two-body collisions and the Pauli principle are important and needed to be included. This leads to

the use of the so-called Vlasov-Uehling-Uhlenbeck (VUU) or Boltzmann-Uehling-Uhlenbeck (BUU) equation, which governs the time evolution of the one-body distibution function $f(\vec{r}, \vec{p}, t)$ in phase space. The non-relativistic form of this equation resembles very much Eq. 27. At incident energies of 1 - 2 AGeV the colliding system contains not only nucleons but also π, η, K and Δ particles as well as higher baryon resonances (N(1440), N(1520), N(1535)). Also strange baryons like Λ, Λ(1405) and Σ may be of importance for studying strangeness degrees of freedom. Therefore, distibution functions f and evolution equations need to be introduced for each type of particles and their coupling as well.

The BUU equation is usually solved by the test-particle method. Here the continuous one-body distribution function f at $t = 0$ is represented by an ensemble of $n \cdot (A_p + A_t)$ pointlike particles, where A_p and A_t denote the number of nucleons contained in the projectile and the target, respectively. The left part of the BUU equation can be regarded as the transport equation for a distribution of classical particles whose propagation in the mean-field is given by the Hamilton's equations of motion:

$$\dot{\vec{p_i}} = -\frac{\partial \langle H \rangle}{\partial \vec{r_i}}, \qquad \dot{\vec{r_i}} = \frac{\partial \langle H \rangle}{\partial \vec{p_i}}, \tag{31}$$

where $\langle H \rangle = \sum_i \frac{p_i^2}{2m_i} + \frac{1}{2}\sum_{i \neq j} V_{ij}$.

The two-body collisions (the right part Eq. 27 or the Uehling-Uhlenbeck part) are treated by Monte-Carlo procedures. BUU type models succeeded in the description of one-body observables like collective flow and particle production. However, phenomena like fragment formation and two-particle correlations in relativistic heavy-ion collisions cannot be calculated in the frame of BUU type models, since they are intimately connected to many-body correlations of particles and fluctuations.

A.2 QMD models

To solve these problems one considers N-particle correlations and N-particle distributions explicitly. This can be done within an approach which is called *quantum molecular dynamics* (QMD). In the QMD model each particle i is represented by a Gaussian wave packet in both space and momentum. From these packets the total N-particle distribution function results by superposition

$$f(\vec{r}, \vec{p}, t) = \sum_i^N f_i(\vec{r_i}, \vec{p_i}, t).$$ (32)

The centre of momentum of each Gaussian $f_i(\vec{r_i}, \vec{p_i}, t)$ is propagated under the influence of potential according to the classical Hamiltonian equations of motion. Hard N-N collisions are included in QMD models by employing a collision term. Two particles collide if their minimum distance d in their centre of mass frame fulfils the requirement:

$$d \le d_0 = \sqrt{\frac{\sigma_{tot}}{\pi}},$$ (33)

where the cross section is assumed to be the free cross section of the regarded collision type (N-N, N-Δ, N-π,...). In addition, the Pauli blocking of particles is taken into account by checking the phase space densities in the final states of a two-body collision. Meson creation and absorption can be treated via resonance processes or inelastic $2 \leftrightarrow 3$ collisions; rescattering can happen at every hadron species.

Isospin can be treated explicitly leading to the so-called *Isospin Quantum Molecular Dynamics* (IQMD) model. Also, relativistic effects are expected to become important in heavy-ion collisions at high energies. In the usual microscopic transport models like BUU and QMD the kinematics is already relativistic but the interactions are usually treated non-relativistically, which breaks the Lorentz covariance. The frame dependence of the transport model has only been addressed in the *relativistic quantum molecular dynamics* (RQMD) and *ultra-relativistic quantum molecular dynamics* (UrQMD) models by the use of Hamiltonian dynamics that is constrained by Poincaré invariance. The meson-exchange nature of N-N interactions, by which the nucleon mean-field potential can be separated into different Lorentz components (e.g. scalar and vector potentials) has been included in the *relativistic BUU approach* (RBUU) and *Hadron-String Dynamics* (HSD) approach. For details of these models we refer the interested reader to [1].

Acknowledgements

I would like to thank

References

[1] W. Cassing, E.L. Bratkovskaya, Phys. Rept. 308 (1999) 65.

[2] G.E. Brown, M. Rho, Phys. Rev. Lett. 66 (1991) 2720.

[3] E.L. Bratkovskaya, W. Cassing, C. Greiner, M. Effenberger, U. Mosel, A. Sibirtsev, Nucl. Phys. A 675 (2000) 661.

[4] B. Kämpfer, O. Pavlenko, Eur. Phys. J. A 10 (2001) 101.

[5] G. Agakichiev et al., Nucl. Phys. A 610 (1996) 317c.

[6] G. Agakichiev et al., Phys.Lett. B 422 (1998) 405.

[7] G.Q. Li, C.M. Ko and G.E. Brown, Phys. Rev. Lett. 75 (1995) 4007.

[8] W. Cassing, W. Ehehalt and C.M. Ko, Phys. Lett. B 363 (1995) 35.

[9] J. Sollfrank et al., Preprint nucl-th/9607029 (1996).

[10] B. Kämpfer, O.P. Pavlenko, K. Gallmeister, Phys. Lett. B 419 (1998) 412.

[11] E.L. Bratkovskaya et al., Nucl. Phys. A 634 (1998) 168.

[12] R.J. Porter et al., Phys. Rev. Lett. 79 (1997) 1229.

[13] J. Ritman, Measurement of the ω meson transition form factor by measuring the reaction $\pi^+ p \rightarrow \pi^+ p \omega$ with the HADES spectrometer, II. Phys. Inst. Gießen, September 15, 2000.

[14] HADES proposal, http://www-hades.gsi.de/internal/May2001/proposal_fin.pdf

[15] F. Sauli, Principles of operation of multiwire proportional and drift chambers, Geneva, 1977.

[16] A. Borghesi et al., Nucl. Instr. Meth. A 153 (1978) 379.

[17] M. Cavalli-Sforza et al., Nucl. Instr. Meth. A 124 (1975) 73.

[18] http:/www.pspice.com

[19] http://www-hades.gsi.de/proceedings/collmeetXI/jboy1/jboy1.html

[20] R. Stephenson et al., Nucl. Instr. Meth. A 171 (1980) 337.

[21] K. B. Burns et al., Nucl. Instr. Meth. A 106 (1973) 171.

[22] D. Carlsmith et al., Nucl. Instr. Meth. A 364 (1988) 550.

[23] L. S. Durkin et al., IEEE Trans. on Nuclear Science, Vol. 42, No. 4, August 1995.